

Energetics and Structural Properties of Trapped Two-Component Fermi Gases

J. von Stecher and Chris H. Greene

Department of Physics and JILA, University of Colorado, Boulder, CO 80309-0440

D. Blume

JILA, University of Colorado, Boulder, CO 80309-0440 and

Department of Physics and Astronomy, Washington State University, Pullman, Washington 99164-2814

(Dated: October 24, 2018)

Using two different numerical methods, we study the behavior of two-component Fermi gases interacting through short-range s -wave interactions in a harmonic trap. A correlated Gaussian basis-set expansion technique is used to determine the energies and structural properties, i.e., the radial one-body densities and pair distribution functions, for small systems with either even or odd N , as functions of the s -wave scattering length and the mass ratio κ of the two species. Particular emphasis is put on a discussion of the angular momentum of the system in the BEC-BCS crossover regime. At unitarity, the excitation spectrum of the four-particle system with total angular momentum $L = 0$ is calculated as a function of the mass ratio κ . The results are analyzed from a hyperspherical perspective, which offers new insights into the problem. Additionally, fixed-node diffusion Monte Carlo calculations are performed for equal-mass Fermi gases with up to $N = 30$ atoms. We focus on the odd-even oscillations of the ground state energy of the equal-mass unitary system having up to $N = 30$ particles, which are related to the excitation gap of the system. Furthermore, we present a detailed analysis of the structural properties of these systems.

PACS numbers:

I. INTRODUCTION

Pure Fermi systems with essentially any interaction strength can be realized experimentally with ultracold atomic gases. In most experiments to date, large samples of atomic Li or K are trapped optically in two different hyperfine states, in the following simply referred to as “spin-up” and “spin-down” states. By tuning an external magnetic field in the vicinity of a Fano-Feshbach resonance [1, 2, 3, 4], the interspecies s -wave scattering length can be varied from non-interacting to infinitely strongly-interacting (either attractive or repulsive). This tunability is unique to atomic systems, and it has enabled for the first time quantitative experimental studies of the crossover from the molecular BEC-regime to the atomic BCS-regime [5, 6, 7, 8, 9, 10]. Since the systems studied experimentally are in general large, many observations have been explained quite successfully by applying theoretical treatments based on the local density approximation (LDA); see, e.g., Ref. [11] and references therein. The LDA uses the equation of state of the homogeneous system as input, and, in general, accurately describes the properties of the system near the trap center, where the density changes slowly. However, it fails to accurately describe the properties of the system near the edge of the cloud, where the density varies more rapidly.

In a different set of experiments, atomic Fermi gases are loaded into an optical lattice with variable barrier height [12, 13, 14]. In the regime where the tunneling of atoms between neighboring lattice sites can be neglected, each lattice site provides an approximately harmonic confining potential for the atoms at that site. Through the application of a so-called “purification scheme” [15], ex-

perimentalists are now able to realize systems with a deterministic number of atoms per site. So far, optical lattices have been prepared with one or zero atoms per site, with two or zero atoms per site, and with three or zero atoms per site. Optical-lattice experiments thus allow for the simultaneous preparation of multiple copies of identical few-particle systems. We anticipate that these experiments will be extended to larger atom samples in the future, thereby opening the possibility to study systematically how the properties of the system change as functions of the number of atoms. Transitions from few- to many-body systems have, e. g., been studied experimentally in metal and rare gas clusters [16, 17], and it is exciting that the experimental study of this transition in dilute gaseous systems is within reach. A mature body of theoretical work has also investigated the manner in which bulk electronic, magnetic and superfluid properties can be understood by studying small or modest-size clusters [18, 19].

This paper presents theoretical results for trapped two-component Fermi gases with up to $N = 30$ fermions, which shed light on the few- to many-body transition from a microscopic or few-body point of view. To solve the many-body Schrödinger equation we use two different numerical methods, a correlated Gaussian (CG) basis set expansion approach and a fixed-node diffusion Monte Carlo (FN-DMC) approach. The CG approach allows for the determination of the entire energy spectrum and eigenstates with controlled accuracy (i.e., no approximations are employed and the convergence can be systematically improved). If we demand an accuracy of the order of 2% or better, our current CG implementation limits us to treating systems with up to $N = 6$ atoms (and to the lowest 10 or twenty eigen states). To the best of

our knowledge, no other such calculations exist for dilute fermionic few-body systems ($N = 4 - 6$) with short-range interactions. The FN-DMC method, in contrast, can be applied to larger systems but its accuracy crucially depends on the quality of the many-body nodal surface, which is in general unknown. Moreover, the FN-DMC approach as implemented here treats only ground state properties for the chosen symmetry. Careful comparisons of the ground state energy and structural properties calculated by the FN-DMC and CG approach for different interaction strengths validate the construction of the nodal surfaces employed for $N \leq 6$. We expect, and provide some evidence, that our nodal surfaces constructed to describe the energetically lowest-lying gas-like state of larger N are also quite accurate.

Specifically, we calculate the energy of the energetically lowest-lying gas-like state of trapped two-species Fermi gases as a function of the number of particles N , the s -wave scattering length a_s and the mass ratio κ . Our ground state energies for even and odd N can be readily combined to determine the excitation gap, which is related to pairing physics. For small systems, we additionally determine and discuss the excitation spectrum. Furthermore, we present pair correlation functions, which provide further insights into the pair formation process, and radial density profiles for the ground state. Finally, we elaborate on the interpretation of the behaviors within a framework that uses hyperspherical coordinates. This connection has been summarized in an earlier paper [20]. Here, we present additional results and discuss in more detail how the even-odd oscillations emerge in the hyperspherical framework. Our analysis provides an alternative means, complementary to conventional many-body theory, for understanding the excitation gap at unitarity.

The remainder of this paper is organized as follows. Section II introduces the Hamiltonian of the system under study, reviews the definitions of the normalized energy crossover curve and the excitation gap, and summarizes some peculiar properties of the unitary gas using hyperspherical coordinates. Section III summarizes the CG and FN-DMC approaches, and provides some implementation details specific to the problem at hand. Section IV presents our results for the ground state energies, the excitation spectrum and structural properties. Finally, Sec. V concludes.

II. THEORETICAL BACKGROUND

A. Hamiltonian

The main objective of this article is to obtain and interpret solutions to the many-body time-independent Schrödinger equation for a trapped two-component Fermi gas with short-range interactions. The model Hamiltonian for N_1 fermions of mass m_1 and N_2 fermions of mass

m_2 reads

$$H = \sum_{i=1}^{N_1} \left(\frac{-\hbar^2}{2m_1} \nabla_i^2 + \frac{1}{2} m_1 \omega^2 \vec{r}_i^2 \right) + \sum_{i'=1}^{N_2} \left(\frac{-\hbar^2}{2m_2} \nabla_{i'}^2 + \frac{1}{2} m_2 \omega^2 \vec{r}_{i'}^2 \right) + \sum_{i=1}^{N_1} \sum_{i'=1}^{N_2} V_0(r_{ii'}). \quad (1)$$

Here, \vec{r}_i and $\vec{r}_{i'}$ denote the position vector of the i th mass m_1 fermion and the i' th mass m_2 fermion, respectively. Both atom species experience a trapping potential characterized by the same angular frequency ω . For equal masses, this is indeed the case in ongoing experiments. For unequal masses, however, the two atomic species typically experience different trapping frequencies. Our restriction to equal trapping frequencies reduces the parameter space which otherwise would be impractical to explore numerically. Furthermore, our CG calculations simplify for equal trapping frequencies because the center-of-mass and relative motions decouple in this case. The studies presented here for unequal masses but equal frequencies complement our earlier study [21], which treats two-component Fermi gases with unequal masses that experience trapping frequencies ω_1 and ω_2 adjusted so that $m_1\omega_1 = m_2\omega_2$. In Eq. (1), V_0 is a short-range two-body potential between each pair of mass m_1 and mass m_2 atoms. We characterize the strength of V_0 by the s -wave scattering length a_s , which can be varied experimentally through the application of an external magnetic field in the vicinity of a Fano-Feshbach resonance. Here, we model this situation by changing the depth of V_0 ; our results should be applicable to systems with a broad s -wave Fano-Feshbach resonance and vanishingly small p -wave interactions.

The present study considers two-component Fermi gases with either even or odd N , where $N = N_1 + N_2$. Because odd-even oscillations serve as one major subject of this study, we set $N_1 = N_2$ for even N , and $N_1 = N_2 \pm 1$ for odd N . In addition to the scattering length a_s , we vary the mass ratio κ ,

$$\kappa = m_1/m_2. \quad (2)$$

Throughout, we take $m_1 \geq m_2$ so that $\kappa \geq 1$. In most cases, we measure lengths in units of the oscillator length a_{ho} , $a_{ho} = \sqrt{\hbar/(2\mu\omega)}$, which is defined in terms of the reduced mass μ , $\mu = m_1 m_2 / (m_1 + m_2)$.

It has been shown previously [20, 22, 23, 24] that small equal-mass two-component Fermi gases, which interact through short-range two-body potentials with infinitely large a_s that support no s -wave bound state, support no tightly-bound many-body states with negative energy. For unequal mass systems the situation is different [23, 25, 26, 27]. Trimers consisting of two heavy particles and one light particle that interact through short-range potentials support tightly-bound states with negative energy if the mass ratio and the scattering length are sufficiently large. Reference [21] discussed the role of non-universal trimer states for unequal-mass systems in

some detail, and we return to this discussion in Sec. IV A. Throughout this work, we restrict our analysis to gas-like states, consisting of atomic fermions, molecular bosons or both.

To solve the Schrödinger equation for eigenstates of H , we use two different numerical methods: a correlated Gaussian (CG) basis set expansion technique and a fixed-node diffusion Monte Carlo (FN-DMC) technique. For numerical convenience, we utilize different short-range potentials V_0 in our CG and FN-DMC calculations. We adopt a purely attractive Gaussian interaction potential defined as

$$V_0(r) = -d \exp\left(-\frac{r^2}{2R_0^2}\right) \quad (3)$$

in the CG calculations, and a square well interaction potential defined as

$$V_0(r) = \begin{cases} -d & \text{for } r < R_0 \\ 0 & \text{for } r > R_0 \end{cases} \quad (4)$$

in the FN-DMC calculations. For a fixed range R_0 , the potential depth d is adjusted so that the s -wave scattering length a_s takes the desired value. The range R_0 is selected so that $R_0 \ll a_{ho}$. The premise is that the properties of two-component Fermi gases with short-range interactions (or at least the universal state properties) are determined by the s -wave scattering length a_s alone, and independent of the details of the underlying two-body potential if the range R_0 is chosen sufficiently small. Ideally, we would consider the limit $R_0 = 0$. This is, however, impossible within the numerical frameworks employed. Thus, we perform calculations for different finite R_0 , which allows us to approximately extrapolate to the $R_0 = 0$ limit and to estimate the dependence of our results on R_0 , i.e., to estimate the scale of the finite-range effects.

B. Energy crossover curve and excitation gap

The energetically lowest-lying gas-like states of two-component Fermi gases with short-range interactions determine the normalized energy crossover curve $\Lambda_N^{(\kappa)}$ and the excitation gap $\Delta(N)$. To simplify the notation, the energetically lowest-lying gas-like state is referred to as the ground state in this section. The BCS and BEC limits of the crossover can be treated perturbatively. For small $|a_s|$ and $a_s < 0$, the system behaves like a weakly-interacting atomic Fermi gas whose leading order properties beyond the non-interacting degenerate Fermi gas are determined by a_s . For attractive two-body potentials that generate small a_s and $a_s > 0$, in contrast, the system behaves like a weakly-interacting molecular Bose gas whose properties are to leading order determined by a_{dd} , where a_{dd} denotes the dimer-dimer scattering length. (One can also have small, positive a_s with purely repulsive two-body potentials that have no bound molecular

states, but these systems behave quite differently and will not be considered in this paper.) In the strongly-interacting regime (large $|a_s|$), perturbation theory cannot be applied and it is not clear *a priori* whether the system behaves more like an atomic gas or a molecular gas, or like neither of the two.

The definition of the normalized energy crossover curve $\Lambda_{N_1, N_2}^{(\kappa)}$ introduced in Refs. [21, 28] for even N can be extended to odd N ,

$$\Lambda_{N_1, N_2}^{(\kappa)} = \frac{E(N_1, N_2) - N_d E(1, 1) - 3N_f/2\hbar\omega}{E_{NI} - \frac{3}{2}N\hbar\omega}. \quad (5)$$

Here, $E(N_1, N_2)$ denotes the ground state energy of the trapped two-component gas consisting of N_1 fermions with mass m_1 and N_2 fermions with mass m_2 . In Eq. (5), N_d is defined by

$$N_d = \min\{N_1, N_2\}, \quad (6)$$

and corresponds to the number of dimers formed on the BEC side, i.e., in the regime where a_s is small and positive. N_f is defined by

$$N_f = |N_1 - N_2|; \quad (7)$$

it represents the number of unpaired atoms on the BEC side, and takes the value 0 for even N and 1 for odd N .

In Eq. (5), E_{NI} denotes the ground state energy of the non-interacting two-component Fermi gas consisting of N atoms, where— as before— $N = N_1 + N_2$. The E_{NI} can be evaluated as the sum of the noninteracting energies of polarized Fermi gases E_{NI}^p with N_1 and N_2 particles, $E_{NI}(N) = E_{NI}^p(N_1) + E_{NI}^p(N_2)$. Following Ref. [29], the $E_{NI}^p(N_i)$ can be written in terms of the shell number n_s , the energy of the closed shell subsystem $E_{NI}^{cs}(n_s)$, and the corresponding magic number N^{cs} ,

$$E_{NI}^p(N_i) = E_{NI}^{cs}(n_s) + \left(\frac{3}{2} + n_s\right)(N - N^{cs})\hbar\omega. \quad (8)$$

The shell number n_s represents the number of closed shells and is given by

$$n_s = \text{Int} \left[\frac{1}{g(N_i)} + \frac{g(N_i)}{3} - 1 \right], \quad (9)$$

where

$$g(N_i) = \sqrt[3]{3 \left(27N_i - \sqrt{3(243N_i^2 - 1)} \right)} \quad (10)$$

and $\text{Int}[x]$ is the integer part of x . Finally, the energy of the closed shell subsystem $E_{NI}^{cs}(n_s)$ and the corresponding magic number N^{cs} are

$$N^{cs} = \frac{n_s(n_s + 1)(n_s + 2)}{6} \quad \text{and} \quad (11)$$

$$\frac{E_{NI}^{cs}(n_s)}{\hbar\omega} = \frac{(n_s - 1)n_s(n_s + 1)(n_s + 2)}{8} + \frac{3N^{cs}}{2}. \quad (12)$$

On the positive a_s side where a high-lying two-body bound state exists, a significant fraction of the ground state energy of the N fermion system is determined by the binding energy of the trapped dimer, which depends on R_0 . To reduce the dependence of $\Lambda_{N_1, N_2}^{(\kappa)}$ on the range R_0 , the energy $E(1, 1)$ of N_d trapped dimer pairs is subtracted in Eq. (5). Thus, $\Lambda_{N_1, N_2}^{(\kappa)}$ depends to a good approximation only on a_s , κ , N_1 and N_2 , and not on the details of the underlying two-body potential (see also Sec. IV A). By construction, $\Lambda_{N_1, N_2}^{(\kappa)}$ changes from one on the weakly-interacting BCS side (small $|a_s|$ and $a_s < 0$) to zero on the weakly-interacting molecular BEC side (small, positive a_s).

The weakly-interacting regimes, where $|a_s| \ll a_{ho}$, can be treated perturbatively assuming zero-range interactions, i.e., a Fermi pseudopotential [30]. For small $|a_s|$ and $a_s < 0$, the energy within first order perturbation theory becomes

$$E \approx E_{NI} + \hbar\omega C_{N_1, N_2}^\kappa \frac{a_s}{a_{ho}}, \quad (13)$$

where C_{N_1, N_2}^κ is a dimensionless quantity. In general, the evaluation of C_{N_1, N_2}^κ is a bit cumbersome since there is no unique ground state and degenerate perturbation theory must be applied. When both N_1 and N_2 correspond to closed shells, then C_{N_1, N_2}^κ can be calculated straightforwardly analytically [21],

$$C_{N_1, N_2}^\kappa = 4\pi a_{ho}^3 \int \rho_1^{NI}(\vec{r}) \rho_2^{NI}(\vec{r}) d\vec{r}. \quad (14)$$

Here, $\rho_i^{NI}(\vec{r})$ is the density of a one-component non-interacting gas with N_i fermions of mass m_i , normalized so that $\int \rho_i^{NI}(\vec{r}) d\vec{r} = N_i$. Alternatively, one can approximate the ρ_i^{NI} by the Thomas-Fermi density profiles. This approximation should be quite accurate in the large N limit.

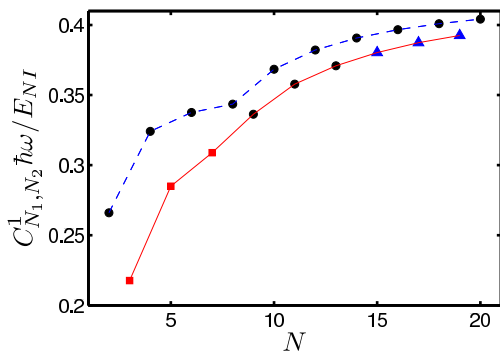


FIG. 1: (Color Online) C_{N_1, N_2}^1 coefficients divided by E_{NI} as a function of N . Circles correspond to $L = 0$ ground state, squares to $L = 1$ ground state and triangles to $L = 2$ ground state. A solid line connects the odd- N values while a dashed line connects the even- N values.

To obtain the C_{N_1, N_2}^κ for open-shell systems, we apply first-order degenerate perturbation theory. This calcula-

TABLE I: Angular momentum L and coefficient C_{N_1, N_2}^1 for the ground state of equal-mass two-component Fermi gases in the weakly-attractive regime. Here, we consider $N_2 = N_1$ for even N and $N_1 = N_2 + 1$ for odd N .

N	L	C_{N_1, N_2}^1	N	L	C_{N_1, N_2}^1
2	0	$\frac{2}{\sqrt{2\pi}}$	12	0	12.2274
3	1	$\frac{3}{\sqrt{2\pi}}$	13	0	13.1651
4	0	$\frac{13}{2\sqrt{2\pi}}$	14	0	15.2382
5	1	$\frac{15}{2\sqrt{2\pi}}$	15	2	16.1642
6	0	$\frac{11}{\sqrt{2\pi}}$	16	0	18.2445
7	1	$\frac{12}{\sqrt{2\pi}}$	17	2	19.1735
8	0	$\frac{31}{2\sqrt{2\pi}}$	18	0	21.2476
9	0	$\frac{145}{8\sqrt{2\pi}}$	19	2	$\frac{1779}{32\sqrt{2\pi}}$
10	0	9.21052	20	0	$\frac{1945}{32\sqrt{2\pi}}$
11	0	10.1980			

tion additionally allows us to obtain the angular momentum quantum number L of the ground state. Figure 1 and Table I present the results for $N \leq 20$ and $\kappa = 1$. The coefficients C_{N_1, N_2}^1 increase monotonically with increasing N and show a slight odd-even staggering. In general, the coefficients C_{N_1, N_2}^1 for even N are comparatively higher than those for odd N , implying a smaller energy for even N than for odd N and suggesting that, even in the perturbative regime, the odd-even oscillations are already present. We note that the C_{N_1, N_2}^1 coefficients for even N shown in Fig. 1 clearly reflect the shell-closure at $N = 8$.

In the weakly-interacting molecular BEC regime, the two-component Fermi system should behave like a system that consists of N_d bosonic molecules and $N_f = 0$ or 1 fermions. In first order perturbation theory the ground state energy of such a system is given by

$$E \approx N_d E(1, 1) + \hbar\omega \frac{3N_f}{2} + \hbar\omega \frac{N_d(N_d - 1)}{2} \sqrt{\frac{2}{\pi}} \frac{a_{dd}}{a_{ho}^{(dd)}} + \hbar\omega N_d N_f \sqrt{\frac{2}{\pi}} \frac{a_{ad}}{a_{ho}^{(ad)}} \quad (15)$$

Here, a_{dd} and a_{ad} denote the dimer-dimer and atom-dimer scattering lengths, respectively. The oscillator lengths $a_{ho}^{(dd)}$ and $a_{ho}^{(ad)}$ for the dimer-dimer and atom-dimer systems, $a_{ho}^{(dd)} = \sqrt{\hbar/(2\mu_{dd}\omega)}$ and $a_{ho}^{(ad)} = \sqrt{\hbar/(2\mu_{ad}\omega)}$, are defined in terms of the reduced mass μ_{dd} of the dimer-dimer system and the reduced mass μ_{ad} of the atom-dimer system, respectively.

The limiting behaviors of the BEC-BCS crossover curve can be used to guide the construction of the many-body nodal surface, which is a crucial ingredient for our FN-DMC calculations (see Sec. III B). In the weakly-interacting molecular BEC regime, even N systems consist of $N/2$ dimers. Each molecule is expected to be in

its rotational ground state, leading to a many-body wave function with total angular momentum $L = 0$. For odd N systems, the extra fermion is expected to occupy the lowest s -wave orbital, leading, as in the even N case, to a many-body wave function with $L = 0$. Thus, the angular momentum of even N systems is expected to be the same along the crossover while that of odd N systems is expected to change (for $N = 3$, this has been pointed out recently by two independent groups [31, 32]). This symmetry change introduces a kink in the normalized energy curve $\Lambda_{N_1, N_2}^{(\kappa)}$ for odd N and in the excitation gap $\Delta(N)$ (see below) at the scattering length where the symmetry change or inversion occurs.

In addition to the energy crossover curve, we calculate the excitation gap $\Delta(N)$, which characterizes the odd-even oscillations of two-component Fermi systems, as a function of N . For homogeneous two-component Fermi systems with equal masses, the excitation gap Δ , which equals half the energy it takes to break a pair, is quite well understood. In the weakly interacting BCS regime, the excitation gap Δ becomes exponentially small [33, 34], indicating vanishingly little pairing. In the deep BEC regime, on the other hand, the excitation gap approaches half the binding energy of the free-space dimer, indicating essentially complete pairing: By adding an extra particle to the odd N system, the energy of the total system changes by approximately the binding energy of the free-space dimer. In addition to these limiting cases, the excitation gap of the equal-mass two-component Fermi system has been determined throughout the crossover regime by the FN-DMC method [35, 36, 37]. For unequal-mass systems, in contrast, the behavior of the gap is much less studied and understood [38, 39, 40, 41, 42].

To define the excitation gap $\Delta(N)$ for trapped unequal-mass systems, we set $N = 2n + 1$ and assume N to be odd. The unequal-mass system is characterized by two chemical potentials, the chemical potential $\mu_1(N)$ for species one and the chemical potential $\mu_2(N)$ for species two (see, *e.g.*, Ref. [43]),

$$E(n + 1, n) = E(n, n) + \mu_1(2n + 1) + \Delta(2n + 1) \quad (16)$$

and

$$E(n, n + 1) = E(n, n) + \mu_2(2n + 1) + \Delta(2n + 1). \quad (17)$$

Here, $\Delta(2n + 1)$ denotes the excitation gap. If $\Delta(2n + 1)$ vanishes— as is the case for the normal system—, then Eqs. (16) and (17) reduce to the “usual” chemical potentials. Furthermore, $\mu_1(N)$ and $\mu_2(N)$ coincide for equal-mass systems. To determine $\mu_1(N)$, $\mu_2(N)$ and $\Delta(N)$, we need an additional relationship. In condensed matter physics, one typically considers the average of the two chemical potentials,

$$\begin{aligned} \frac{1}{2} [\mu_1(2n + 1) + \mu_2(2n + 1)] = \\ \frac{1}{2} [E(n + 1, n + 1) - E(n, n)]. \end{aligned} \quad (18)$$

Since the average chemical potential is defined in terms of the energy of the next smaller and the next larger balanced systems, it is independent of the odd-even oscillations. Equations (16) through (18) can be solved for $\mu_1(2n + 1)$, $\mu_2(2n + 1)$ and $\Delta(2n + 1)$,

$$\begin{aligned} \mu_1(2n + 1) = \frac{E(n + 1, n + 1) - E(n, n + 1)}{2} \\ + \frac{E(n + 1, n) - E(n, n)}{2}, \end{aligned} \quad (19)$$

$$\begin{aligned} \mu_2(2n + 1) = \frac{E(n + 1, n + 1) - E(n + 1, n)}{2} \\ + \frac{E(n, n + 1) - E(n, n)}{2}, \end{aligned} \quad (20)$$

and

$$\begin{aligned} \Delta(2n + 1) = \frac{E(n + 1, n) + E(n, n + 1)}{2} \\ - \frac{E(n, n) + E(n + 1, n + 1)}{2}. \end{aligned} \quad (21)$$

Note that the energies $E(n + 1, n)$ and $E(n, n + 1)$ are equal for equal masses. The excitation gap $\Delta(N)$ and the chemical potentials $\mu_1(N)$ and $\mu_2(N)$ depend on N , κ , ω and a_s .

Ultimately, one of the goals is to relate the excitation gaps calculated for the trapped and the homogeneous systems. For equal masses and equal frequencies, the densities of the two trapped species overlap fully. Hence, one might expect that the excitation gaps of the homogeneous and inhomogeneous systems can be related via the local density approximation (LDA), which predicts that $\Delta(N)$ scales with N as $N^{1/3}$. Connecting the excitation gaps for the homogeneous and trapped systems in this way breaks down, however, if the extra particle sits near the edge of the gas cloud; this is the region that is poorly described by the LDA. Indeed, we present some evidence that the extra particle sits for $N \gtrsim 11$ near the cloud edge. For unequal masses, the connection between the two excitation gaps becomes even more challenging, because one now has to first determine whether the trapped system exhibits phase separation or not [40, 44].

For the trapped system, the density mismatch can be quantified by comparing the density overlap O_{N_1, N_2}^κ ,

$$O_{N_1, N_2}^\kappa = a_{ho}^3 \int \rho_1(\vec{r}) \rho_2(\vec{r}) d\vec{r}, \quad (22)$$

of the unequal-mass system with that of the equal-mass system for a given scattering length a_s . In Eq. (22), the one-body densities $\rho_i(\vec{r})$ and the oscillator length a_{ho} depend on κ . In the non-interacting limit, the normalized density mismatch $O_{N_1, N_2}^\kappa / O_{N_1, N_2}^1$ reduces to $C_{N_1, N_2}^\kappa / C_{N_1, N_2}^1$. In this case, $O_{N_1, N_2}^\kappa / O_{N_1, N_2}^1$ equals one for all κ if $N_1 = N_2 = 1$ (see Table II of Ref. [21]). For larger N , however, $O_{N_1, N_2}^\kappa / O_{N_1, N_2}^1$ decreases from 1 to a finite value that is smaller than one as κ varies from

one to infinity. In particular, the Thomas Fermi approximation predicts $O_{N_1, N_2}^\kappa / O_{N_1, N_2}^1 = 315\pi/1024\sqrt{2} \approx 0.683$ for large non-interacting systems ($N_1 = N_2$) with large κ . For the small unequal-mass systems considered in Sec. IV, we find that the density mismatch for finite a_s is smaller than that for $a_s = 0$.

C. Hyperspherical formulation at unitarity

The two-component Fermi gas at unitarity is characterized by a diverging scattering length, i.e., $1/a_s = 0$. In this regime, the underlying two-body potential, for sufficiently small R_0 , has no characteristic length scale, thus leaving only the size of the system itself. This elimination of the two-body length scale is the key to obtaining a number of analytical results; a particularly appealing framework for deriving these results employs hyperspherical coordinates. The hyperspherical formulation has been primarily developed in the context of few-body systems [45, 46, 47, 48, 49, 50]. More recently, some properties of Bose and Fermi gases with essentially arbitrary number of atoms have been explained successfully within this formulation [51, 52, 53]. The ability to treat both small and large systems on equal footing makes the hyperspherical formulation particularly suited for studying the transition from few- to many-body systems.

We define the hyperspherical coordinates by first separating off the center-of-mass vector \vec{R}_{CM} , and by then dividing the remaining $3N - 3$ coordinates into the hyperradius R and $3N - 4$ hyperangles, collectively denoted by Ω . The hyperradius R is defined by

$$\mu_N R^2 = \sum_{i=1}^{N_1} m_1 r_i^2 + \sum_{i'=1}^{N_2} m_2 r_{i'}^2 - M R_{CM}^2, \quad (23)$$

and can be viewed as a coordinate that measures the overall size of the system. Here, M denotes the total mass of the system, $M = m_1 N_1 + m_2 N_2$, and μ_N an arbitrary mass scaling factor. Usually, the value of μ_N is chosen so that the hyperradial potential curves $V_{s_\nu}(R)$, defined below, approach physically motivated asymptotic values as $R \rightarrow \infty$.

In the adiabatic approximation [47], the relative wave function $\Psi^{rel}(R, \Omega)$ reduces to

$$\Psi^{rel}(R, \Omega) = R^{-(3N-4)/2} F_{\nu n}(R) \Phi_\nu(R; \Omega). \quad (24)$$

The antisymmetric Pauli correlations are built into the channel functions $\Phi_\nu(R; \Omega)$ at the outset. In addition, the $\Phi_\nu(R; \Omega)$ account for a significant fraction of the two-body correlations of the system. Within the hyperspherical approximation, the description of the many-body system reduces to solving a one-dimensional Schrödinger equation in the hyperradial coordinate R ,

$$\begin{aligned} \left(-\frac{\hbar^2}{2\mu_N} \frac{d^2}{dR^2} + V_{s_\nu}(R) + \frac{1}{2}\mu_N\omega^2 R^2 \right) F_{\nu n}(R) \\ = E_{\nu n}^{rel} F_{\nu n}(R). \end{aligned} \quad (25)$$

The effective hyperradial potential $V_{s_\nu}(R)$ includes part of the kinetic energy and a contribution due to the short-range two-body interactions.

Assuming zero-range interactions, the adiabatic approximation becomes exact for a subclass of universal states of the unitary two-component Fermi gas [54]. For these states, the channel functions Φ_ν obey specific boundary conditions imposed by the zero-range pseudopotential and become independent of R . Furthermore, the functional form of the hyperradial potentials $V_{s_\nu}(R)$ can be derived analytically [54, 55],

$$V_{s_\nu}(R) = \frac{\hbar^2 s_\nu (s_\nu + 1)}{2\mu_N R^2}. \quad (26)$$

The eigen energies of Eq. (25) are then given by

$$E_{\nu n}^{rel} = \left(s_\nu + 2n + \frac{3}{2} \right) \hbar\omega, \quad (27)$$

where n is a non-negative integer, and the hyperradial wave functions $F_{\nu n}(R)$ (not normalized) by

$$F_{\nu n}(R) = R^{s_\nu+1} L_n^{(s_\nu+1/2)}(R^2/\mathcal{L}^2) \exp\left(-\frac{R^2}{2\mathcal{L}^2}\right), \quad (28)$$

where \mathcal{L} denotes the oscillator length associated with μ_N , $\mathcal{L} = \sqrt{\hbar/(\mu_N\omega)}$, and $L_n^{(s_\nu+1/2)}$ the Laguerre polynomial. The total energy $E_{\nu n}$ is obtained from $E_{\nu n}^{rel}$ by adding the center of mass energy. The spacing between states labeled by the same ν is $2\hbar\omega$ and is thus independent of s_ν . This implies that knowledge of the lowest eigenenergy $E_{\nu 0}^{rel}$ in each hyperradial potential curve determines the entire energy spectrum. This property of the spectrum has also been shown using the scale invariance properties of unitary systems [56]. Transitions between vibrational levels that lie within a given hyperradial potential curve $V_{s_\nu}(R)$ can be driven by an excitation operator that depends on R only. Such a driving field results in a ladder of excitation frequencies of the form $2k\hbar\omega$, where k denotes an integer. On the other hand, transitions between states living in different hyperradial potential curves (labeled by ν and ν') require the driving field to depend on Ω , or stated more generally, the excitation operator must not commute with the fixed-hyperradius Hamiltonian. The corresponding excitation frequencies are, in general, non-integer multiples of $2\hbar\omega$ and depend on the difference between s_ν and $s_{\nu'}$. Thus, knowledge of the entire excitation spectrum requires determining all s_ν . Moreover, the coefficients s_ν of the three-body system play a role in determining the three-body recombination rate for large and negative a_s [57], and the lifetime of weakly bound dimers for large and positive a_s [57]. Similarly, one may expect that the s_ν of larger systems play a role in determining the corresponding quantities for larger systems. Section IV C presents evidence of the $2\hbar\omega$ energy spacing and determines the s_ν coefficients for the four-particle system for various mass ratios.

Equation (23) defines the hyperradius R without the CM motion. Alternatively, we can define a hyperradius R' ,

$$MR'^2 = \mu_N R^2 + MR_{CM}^2, \quad (29)$$

which includes the CM motion and represents the rms radius of the system. In the adiabatic approximation, the total wave function $\Psi(R', \Omega')$ can be written in terms of the new hyperradius R' as $\Psi(R', \Omega') = R'^{-(3N-1)/2} \bar{F}_{\nu n}(R') \bar{\Phi}(R'; \Omega')$, where Ω' collectively denotes the $3N - 1$ hyperangles. Equations (25) and (26) remain valid if R , μ_N and $F_{\nu n}$ are replaced by R' , M and $\bar{F}_{\nu n}$, respectively. The eigen values of the hyperradial Schrödinger equation equal the eigenenergies $E_{\nu n}$ of the total system. Defining $x = R'/R'_{NI}$ and $\epsilon_{\nu n} = E_{\nu n}/E_{NI}$, the hyperradial Schrödinger equation can be rewritten as

$$\left(-\frac{1}{2\mu_{eff}} \frac{d^2}{dx^2} + \frac{s_\nu(s_\nu + 1)}{2\mu_{eff}x^2} + \frac{1}{2}x^2 \right) \bar{F}_{\nu n}(x) = \epsilon_{\nu n} \bar{F}_{\nu n}(x), \quad (30)$$

where $\mu_{eff} = E_{NI}^2/(\hbar\omega)^2$. Above, R'_{NI} denotes the rms radius of the non-interacting system; it can be, using the virial theorem [54, 58], expressed in terms of the energy E_{NI} of the non-interacting two-component Fermi gas,

$$R'_{NI} = \sqrt{\langle R^2 \rangle_{NI}} = \sqrt{\frac{\hbar}{M\omega}} \sqrt{\frac{E_{NI}}{\hbar\omega}}. \quad (31)$$

The dimensionless coefficients \bar{C}_N ,

$$\bar{C}_N = \frac{s_0(s_0 + 1)}{\mu_{eff}} = \frac{s_0(s_0 + 1)\hbar^2\omega^2}{E_{NI}^2}, \quad (32)$$

characterize the ground state of the system at unitarity. The scaled hyperradius x and the scaled energies $\epsilon_{\nu n}$ remain finite in the large N limit and are thus particularly well suited to discuss the large N limit (see Sec. IV B). For small systems, in contrast, some properties of the system can be highlighted more naturally using the unscaled hyperradius R or R' .

The coefficients s_ν describe both the trapped and free systems, and can be related to the universal parameter ξ of the homogeneous system [20]. The hyperspherical framework thus connects few- and many-body quantities and allows one to bridge the gap between atomic and condensed matter physics.

III. NUMERICAL TECHNIQUES

A. Correlated Gaussian approach

The CG method has proven capable of providing an accurate description of trapped few-body systems with short-range interactions [20, 21, 59]. The CG method

expands the many-body wave function Ψ in terms of a set of basis functions $\Phi_{\{d_{ij}\}}$,

$$\Psi(\vec{r}_1, \dots, \vec{r}_N) = \sum_{\{d_{ij}\}} C_{\{d_{ij}\}} \Phi_{\{d_{ij}\}}(\vec{r}_1, \dots, \vec{r}_N), \quad (33)$$

where the $C_{\{d_{ij}\}}$ denote expansion coefficients and the $\{d_{ij}\}$ a set of widths. Each basis function has the form:

$$\Phi_{\{d_{ij}\}} = \mathcal{S} \left\{ \psi_0(\vec{R}_{CM}) \exp \left(- \sum_{j>i=1}^N r_{ij}^2 / (2d_{ij}^2) \right) \right\}. \quad (34)$$

Here, ψ_0 is the ground state wavefunction associated with the center-of-mass vector \vec{R}_{CM} , and the operator \mathcal{S} ensures that the basis functions have the proper symmetry under exchange of two fermions of the same species. Due to the simplicity of the basis functions, the elements of the Hamiltonian and overlap matrices can be calculated analytically [60, 61]. Since the basis functions depend only on the center of mass vector and the interparticle distances, i.e., Gaussians centered around $r_{ij} = 0$, the resulting eigenenergies correspond to eigenstates with zero relative angular momentum L_{rel} and zero total angular momentum L ; throughout this work, we do not consider center-of-mass excitations so that $L_{rel} = L$ for all systems investigated. To determine the eigenenergies of states of the N -atom system with non-vanishing L_{rel} , we add a spectator atom and solve the Schrödinger equation for the $(N+1)$ -atom system. The extra particle does not interact with the rest of the system but can have non-vanishing angular momentum. This trick allows us to describe non-zero angular momentum states of the N -atom system. We find, e.g., that the ground state of the equal-mass three- and five-particle systems at unitarity has $L_{rel} = 1$.

To illustrate how the energies calculated by the CG method converge with respect to the size of the basis set, we consider the three-body system with $L = 0$ at unitarity. We define E_D as the eigenenergies obtained for an optimized basis set of size D . The optimization of the basis functions for a given size D is performed using the basic ideas of the stochastic variational approach [61]. The size of the basis set is then increased and the new basis functions are optimized. Figure 2 shows an example of the convergence of the lowest few eigenenergies for $R_0 = 0.01a_{ho}$ as a function of D . The largest D considered in this study is 700, and the energies have been tested and are approximately converged for this D value. Thus, Fig. 2 shows the normalized difference between E_{700} and E_D for the lowest few eigenenergies. Figure 2 shows that the basis set can be improved systematically.

For larger number of particles, the size of the basis set needs to be increased. For $N = 5$ and 6, the size of the basis set is increased up to approximately $D = 10^4$. The $N = 6$ energies reported in Ref. [20], e.g., are calculated for $D = 1.6 \times 10^4$. Here, we analyze the convergence of these energies as a function of $1/D$. Since

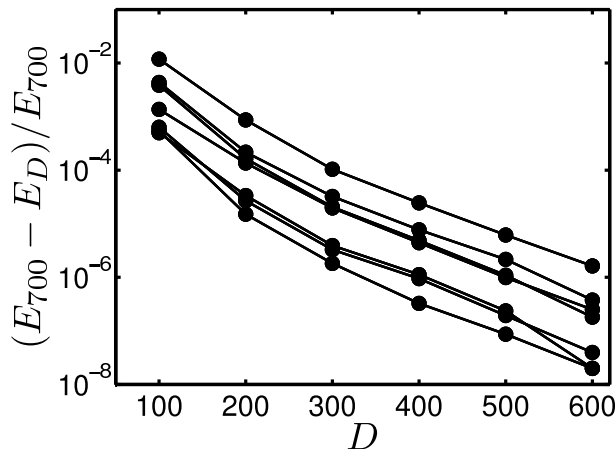


FIG. 2: Convergence of the energetically lowest-lying energies as a function of the size D of the basis set for $N = 3$ ($L = 0$) at unitarity. The range R_0 is fixed at $0.01a_{ho}$. Solid lines connect the CG energies (filled circles) of a given state for ease of viewing.

the energies behave approximately linearly as a function $1/D$, we can extrapolate straightforwardly to the limit $D \rightarrow \infty$. The extrapolated energies for $\nu = 0$ are $E_{00} = 8.48\hbar\omega$, $E_{01} = 10.50\hbar\omega$ and $E_{02} = 12.50\hbar\omega$. E_{00} and E_{01} agree with those reported in Ref. [20] for $D = 1.6 \times 10^4$ while E_{02} is only $0.02\hbar\omega$ lower than the previously reported value. For $\nu = 1$ and 2, the extrapolated energies are $E_{10} = 10.43\hbar\omega$ and $E_{20} = 10.99\hbar\omega$; these energies are lower by $0.01\hbar\omega$ than those reported in Ref. [20]. While the extrapolated energies are most likely closer to the exact eigenenergies than the energies calculated for $D = 1.6 \times 10^4$, we note that the extrapolated energies are no longer variational, i.e., they no longer provide upper bounds to the exact eigenenergies. Our analysis of the $\nu \leq 2$ excited energies shows that the extrapolated energies follow the expected $2\hbar\omega$ spacing more closely than those calculated for the largest D considered, suggesting that the extrapolation procedure is indeed justified.

In general, the convergence of the energies with respect to the basis set depends on the scattering length a_s and the number of states considered. Usually, an accurate determination of the spectrum at unitarity requires a larger basis than the determination of the spectrum on both the weakly-interacting BEC and BCS sides. For equal-mass systems, a converged basis at unitarity usually describes the spectrum in the entire crossover region accurately. Of the equal-mass systems treated, the $N = 5$ ($L = 1$) calculations have been the hardest to converge. For $L = 1$ states, we can estimate the uncertainty of the calculations by monitoring the energy of the spare non-interacting particle, which is known analytically. For example, for the $N = 5$ equal-mass calculations presented in Ref. [20], the energies of the spare non-interacting particle deviate from the exact solution by approximately $0.01\hbar\omega$, which is less than 1%. We find

that systems with large κ are typically harder to converge than the corresponding equal-mass systems.

To analyze the effects of finite range interactions we study the eigenenergies of the three-particle system at unitarity ($L = 0$) as a function of the range R_0 . Figures 3(a) through (c) show the energies for the low-

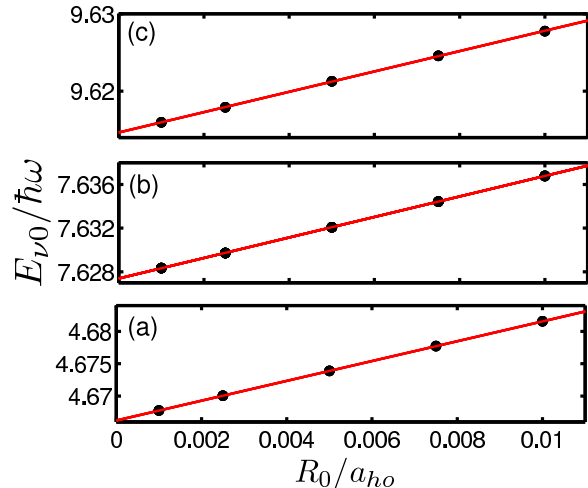


FIG. 3: (Color Online) Three-body energies $E_{\nu 0}$ at unitarity for $L = 0$ [(a) $\nu = 0$, (b) $\nu = 1$ and (c) $\nu = 2$] as a function of the range R_0 . Symbols show the CG energies and solid lines the linear extrapolation to the $R_0 = 0$ limit.

est state in the hyperradial potential curve $V_{s_\nu}(R)$ with $\nu = 0, 1$ and 2. The energies show a linear dependence on R_0 , and can thus be extrapolated straightforwardly to the zero range limit. Neglecting the basis set error, which is estimated to be smaller than the uncertainty of the extrapolation, we find $E_{00} = 4.66622(1)\hbar\omega$, $E_{10} = 7.62738(2)\hbar\omega$, and $E_{20} = 9.61466(4)\hbar\omega$. Our three-body energies compare favorably with those calculated using the s_ν coefficients, $\nu = 0$ and 1, determined by Ref. [57] in Eq. (27), $E_{00} = 4.6662220\hbar\omega$ and $E_{10} = 7.6273521\hbar\omega$. Section IV A reports three-particle energies for equal masses for $R_0 = 0.01a_{ho}$, which— according to Fig. 3— agree to better than $0.02\hbar\omega$ with those calculated in the zero-range limit. We additionally performed systematic studies of the dependence of the energies on the range R_0 for the three-body system with equal and unequal masses in the weakly-interacting molecular BEC regime, where two-body bound states form (see Secs. II B and IV A), and for the four-body system. For the five- and six-body calculations, it is prohibitively expensive to perform calculations for different R_0 . For these systems, we estimate the finite range effects based on our findings for the $N = 3$ and 4 systems.

In addition to the energies, Sec. IV D reports structural properties calculated by the CG approach. The one-body density and the pair-distribution functions are extracted from the total wave function Ψ calculated by the CG approach by integrating Ψ^2 over the relevant Jacobi coordinates.

B. Fixed-node diffusion Monte Carlo approach

For larger systems, the CG approach in our current implementation becomes prohibitively expensive and we instead determine first-principles solutions of the time-independent Schrödinger equation using Monte Carlo techniques.

In this study, we use the FN-DMC method [62, 63], a variant of the diffusion Monte Carlo (DMC) method, to determine solutions for up to $N = 30$ fermions. The DMC method, which interprets the system's wave function as a density, allows for the accurate determination of the energy of nodeless ground states but is not suited to determine the energy of excited states of bosonic systems or of fermionic systems. To treat systems whose eigenfunctions have nodes, the DMC algorithm has to be modified slightly. Here, we adopt the FN-DMC method, which obtains a solution of the Schrödinger equation that has the same symmetry as a so-called guiding function ψ_T . The FN-DMC method provides, to within statistical uncertainties, an upper bound to the exact eigen energy of the many-boson or many-fermion system, i.e., to the lowest-lying state with the same symmetry as ψ_T .

If the nodal surface of ψ_T coincides with that of the exact eigenfunction, then the FN-DMC method results in the exact eigen energy of the system. In general, however, the nodal surface of the exact eigenfunction is not known and the FN-DMC results depend crucially on the quality of the nodal surface of ψ_T . In this work, we consider three different parametrizations of the nodal surface of two-component Fermi systems.

The guiding function ψ_{T1} reads

$$\psi_{T1} = \prod_{i=1}^{N_1} \Phi_1(\vec{r}_i) \times \prod_{i'=1}^{N_2} \Phi_2(\vec{r}_{i'}) \times F_{node}^{T1}(\vec{r}_1, \dots, \vec{r}_{N_2}) \times \prod_{i < j}^{N_1} g_{11}(r_{ij}) \times \prod_{i' < j'}^{N_2} g_{22}(r_{i'j'}) \times \prod_{i, i'}^{N_1, N_2} g_{12}(r_{ii'}) \quad (35)$$

The function F_{node}^{T1} determines the nodal structure of ψ_{T1} and is, for even N and $N_1 = N_2$, constructed by antisymmetrizing a product of pair functions f [64],

$$F_{node}^{T1} = \mathcal{A}(f(r_{11'}), f(r_{22'}), \dots, f(r_{N_1 N_2})), \quad (36)$$

where \mathcal{A} is the antisymmetrization operator. The pair function f is given by the free-space two-body solution [64]: f coincides with the free-space two-body bound state solution for positive scattering length a_s , and with the free-space scattering solution, calculated at the scattering energy E_{rel} , for negative a_s . For $N = 6$, we treat E_{rel} as a variational parameter and find a reduction of the energy of 1 or 2% for a finite E_{rel} compared to $E_{rel} = 0$. For larger N , we simply use $E_{rel} = 0$. For odd N , we add a single particle orbital ϕ_{nl} in Eq. (36) so

that F_{node}^{T1} becomes, for $N_1 = N_2 + 1$ [35, 65],

$$F_{node}^{T1} = \mathcal{A}(f(r_{11'}), \dots, f(r_{N_1-1, N_2}), \phi_{nl}(\vec{r}_{N_1}/a_{ho}^{(1)})) = \det \begin{pmatrix} f(r_{11'}) & \dots & f(r_{1N_2}) & \phi_{nl}(\vec{r}_1/a_{ho}^{(1)}) \\ f(r_{21'}) & \dots & f(r_{2N_2}) & \phi_{nl}(\vec{r}_2/a_{ho}^{(1)}) \\ \vdots & & \vdots & \vdots \\ f(r_{N_1 1'}) & \dots & f(r_{N_1 N_2}) & \phi_{nl}(\vec{r}_{N_1}/a_{ho}^{(1)}) \end{pmatrix}, \quad (37)$$

where $a_{ho}^{(i)} = \sqrt{\hbar/(m_i \omega)}$. We consider a number of different single particle orbitals ϕ_{nl} , and determine the optimal nl values by performing a series of FN-DMC calculations. For the lowest n and l , the orbitals read $\phi_{00}(\vec{r}/a_{ho}^{(1)}) = 1$, $\phi_{01}(\vec{r}/a_{ho}^{(1)}) = z/a_{ho}^{(1)}$, $\phi_{20}(\vec{r}/a_{ho}^{(1)}) = 1 - 2(r/a_{ho}^{(1)})^2/3$ and $\phi_{02}(\vec{r}/a_{ho}^{(1)}) = 3(z/a_{ho}^{(1)})^2 - (r/a_{ho}^{(1)})^2$.

In Eq. (35), the Φ_i ($i = 1$ and 2) denote Gaussian single particle orbitals that depend on a width parameter b_i , $\Phi_i(\vec{r}) = \exp(-r^2/(2b_i^2))$. If $b_i = \sqrt{\hbar/(m_i \omega)}$, Φ_i coincides with the ground state orbital of the harmonic oscillator. The parameters b_1 and b_2 are optimized variationally. For even N ($N_1 = N_2$) and equal masses, we require $b_1 = b_2$. At unitarity, e.g., we find that the b_i are smaller than the $a_{ho}^{(i)}$, reflecting the attractive nature of the interspecies interaction potential. If $b_i = a_{ho}^{(i)}$, the product $\Phi_i(\vec{r})\phi_{nl}(\vec{r}/a_{ho}^{(i)})$ equals the harmonic oscillator wave function $\phi_{nl0}^{(HO)}(\vec{r}/a_{ho}^{(i)})$.

In Eq. (35), the pair functions g_{11} , g_{22} and g_{12} are introduced to improve the variational energy and to additionally ensure that the structural properties calculated at the VMC and FN-DMC levels agree at least qualitatively. The pair functions g_{11} and g_{22} allow for the effective repulsion between equal fermions to be accounted for,

$$g_{ii}(r) = \exp(-p_i r^{-q_i}) \quad (38)$$

for $i = 1$ and 2 . The parameters p_1 , p_2 , q_1 and q_2 are optimized variationally. For even N and equal masses, we require $p_1 = p_2$ and $q_1 = q_2$. The pair function g_{12} is parametrized in terms of the three variational parameters t , p_{12} and q_{12} ,

$$g_{12}(r) = 1 + t \exp(-p_{12} r^{-q_{12}}). \quad (39)$$

The parameters t , p_{12} and q_{12} are optimized under the constraint that $g_{12} \geq 0$.

The guiding function ψ_{T1} is expected to provide a good description of the system in the weakly-interacting molecular BEC regime, where we expect bound dimer pairs to form. Section IV B shows that this wave function also provides a good description of the unitary gas for sufficiently large N . This is in agreement with FN-DMC studies for the homogeneous system [64]. Since each pair function f has vanishing relative orbital angular momentum, the total angular momentum L of ψ_{T1} is 0 for even

N and $N_1 = N_2$. For odd N , L of ψ_{T1} is determined by the angular momentum of ϕ_{nl} , i.e., $L = l$.

In addition to ψ_{T1} , we consider the guiding function ψ_{T2} ,

$$\psi_{T2} = \prod_{i=1}^{N_1} \Phi_1(\vec{r}_i) \times \prod_{i'=1}^{N_2} \Phi_2(\vec{r}_{i'}) \times \Psi_{node}^{T2}(\vec{r}_1, \dots, \vec{r}_{N_2}) \times \prod_{i,i'}^{N_1, N_2} \bar{f}(r_{ii'}). \quad (40)$$

The nodal surface of ψ_{T2} is determined by Ψ_{node}^{T2} , which is defined so that the product $\prod_{i=1}^{N_1} \Phi_1(\vec{r}_i) \times \prod_{i'=1}^{N_2} \Phi_2(\vec{r}_{i'}) \times \Psi_{node}^{T2}$ coincides for $b_i = a_{ho}^{(i)}$ with the wave function of N trapped non-interacting fermions. Thus, the nodal surface of ψ_{T2} coincides with that of the corresponding non-interacting system. The pair function \bar{f} coincides with the pair function f introduced above for $r \leq R_m$, where R_m is a matching point determined variationally. For $r > R_m$, \bar{f} is given by $c_1 + c_2 \exp(-\alpha r)$. The parameters c_1 and c_2 are determined by the condition that \bar{f} and its derivative be continuous at $r = R_m$ while α is optimized variationally.

The guiding function Ψ_{T2} is expected to provide a good description of the system in the weakly-interacting BCS regime. In this regime, we construct the guiding function so that its angular momentum agrees with that predicted analytically (see Table I). Section IV B shows that the guiding function Ψ_{T2} also provides a good description of small fermionic systems at unitarity.

Finally, the guiding function ψ_{T3} is constructed following Eqs. (3) and (4) of Ref. [66]. We find that ψ_{T3} gives the lowest energy for $N = 11$.

Expectation values $\langle A \rangle$ of operators A that do not commute with the Hamiltonian cannot be calculated as straightforwardly by the FN-DMC method as the energy. Here, we use the mixed estimator $\langle A \rangle_{mixed}$ [63, 67],

$$\langle A \rangle_{mixed} = 2\langle A \rangle_{DMC} - \langle A \rangle_{VMC}. \quad (41)$$

In Eq. (41), $\langle A \rangle_{VMC}$ denotes the expectation value calculated by the VMC method and $\langle A \rangle_{DMC}$ that calculated by the FN-DMC method. We note that some algorithms for the calculation of pure estimators exist [68, 69] but we do not use them in this work.

In some cases, we optimize the variational parameters, collectively denoted by \vec{p} , by not only minimizing the energy expectation value but by additionally ensuring that ψ_T captures selected structural properties correctly. To this end, we compare the structural properties calculated by the VMC method for a given \vec{p}_0 with those obtained by the FN-DMC method, which uses $\psi_T(\vec{p}_0)$ as a guiding function, and then choose a new parameter set \vec{p}_1 so that the VMC structural properties calculated using \vec{p}_1 agree better with the FN-DMC structural properties calculated using \vec{p}_0 . This procedure is repeated till the VMC and FN-DMC structural properties and energy expectation values agree sufficiently well. For equal-mass

TABLE II: Dimer-dimer scattering length a_{dd} and dimer-dimer effective range r_{dd} obtained using (a) the CG spectrum and (b) the FN-DMC energies. The reported uncertainties reflect the uncertainties due to the fitting procedure; the potential limitations of the FN-DMC method to accurately describe the energetically lowest-lying gas-like state, e.g., are not included here (see Sec. IIIB of Ref. [21]).

κ	a_{dd}/a_s (a)	a_{dd}/a_s (b)	r_{dd}/a_s (a)	r_{dd}/a_s (b)
1	0.608(2)	0.64(1)	0.13(2)	0.12(4)
4	0.77(1)	0.79(1)	0.15(1)	0.23(1)
8	0.96(1)	0.98(1)	0.28(1)	0.38(2)
12	1.10(1)	1.08(2)	0.39(2)	0.55(2)
16	1.20(1)	1.21(3)	0.55(2)	0.60(5)
20	1.27(2)	1.26(5)	0.68(2)	0.74(5)

systems with $N \leq 20$, our VMC energies are at most 15% higher than the corresponding FN-DMC energies. The optimization strategy employed here is similar in spirit to that discussed in Ref. [70] for the homogeneous system.

IV. RESULTS

A. Ground state energy in the crossover regime

This section discusses the behavior of the crossover curve and the excitation gap for $N = 3$ for different mass ratios κ . This odd N study complements our earlier results for even N [21]. Our analysis for $N = 4$ showed that the crossover curve $\Lambda_N^{(\kappa)}$ is independent of the details of the two-body potential and allowed us to extract the dimer-dimer scattering length a_{dd} and the dimer-dimer effective range r_{dd} as a function of κ . The a_{dd} and r_{dd} results from Ref. [21] are summarized in Table II. Furthermore, for larger even N systems, we determined the validity regimes of the analytically calculated limiting behaviors in the weakly-interacting molecular BEC and atomic BCS regimes. Our even N study resulted in a deeper understanding of some of the peculiarities of trapped systems and emphasized similarities and differences between the trapped and homogeneous systems.

The behavior of odd N systems is rich and, in many cases, qualitatively different from that of even N systems. One characteristic of odd N systems is the possible change of the angular momentum of the ground state as the scattering length is tuned through the BEC-BCS crossover region (see Sec. IIB and Refs. [31, 32]). Figure 4 shows the three-particle energy E , with the energy $E(1, 1) + 3\hbar\omega/2$ subtracted, for $L = 0$ (solid lines) and $L = 1$ (dashed lines). The upper panel shows results for $\kappa = 1$, and the two lower panels for $\kappa = 4$ [panels (b) and (c) consider the three-particle system with a spare heavy and a spare light particle, respectively]. The ground state has $L = 1$ for $a_{ho}/a_s \rightarrow -\infty$ and $L = 0$

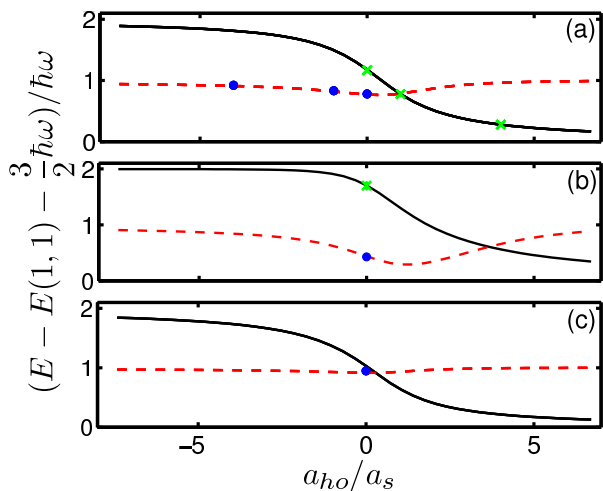


FIG. 4: (Color Online) Normalized energy $(E - E(1,1) - 3\hbar\omega/2)/\hbar\omega$ for $N = 3$ as a function of a_{ho}/a_s calculated by the CG approach (lines). E denotes the three-body energy for $L = 0$ (solid lines) and for $L = 1$ (dashed lines): (a) equal-mass atoms [$\kappa = 1$, $E = E(2,1) = E(1,2)$], (b) two heavy atoms and one light atom [$\kappa = 4$, $E = E(2,1)$], and (c) two light atoms and one heavy atom [$\kappa = 4$, $E = E(1,2)$]. The normalized energy crossover curve $\Lambda_3^{(\kappa)}$, Eq. (5), coincides with the dashed and solid lines, respectively, depending on whether the three-particle ground state has $L = 1$ or 0. In the CG calculations, the range R_0 of the two-body potential is fixed at $0.01a_{ho}$. For comparison, crosses and circles show selected FN-DMC energies for $L = 0$ and $L = 1$, respectively.

for $a_{ho}/a_s \rightarrow \infty$, independent of κ and independent of whether the spare particle is heavy or light. For equal masses, the change of symmetry occurs at $a_s \approx a_{ho}$. For $\kappa = 4$, in contrast, it occurs at $a_s \approx 0.3a_{ho}$ if the extra particle is a heavy atom [panel (b)] and at $a_s \approx 3a_{ho}$ if the extra particle is a light atom [panel (c)]. The dashed and solid lines shown in Fig. 4 coincide with the normalized crossover curve $\Lambda_{N_1, N_2}^{(\kappa)}$, Eq. (5), in the region where the ground state of the three-particle system has $L = 1$ and 0, respectively. The normalized crossover curve $\Lambda_3^{(\kappa)}$ changes from 1 in the weakly-interacting molecular BEC regime to 0 in the weakly-interacting BCS regime.

We find that the normalized $L = 1$ energy curve for two heavy atoms and one light atom [Fig. 4(b)] depends notably on the range of the underlying two-body potential if the scattering length a_s is positive. For example, the normalized energy curve changes by as much as 20% if the range R_0 of the two-body potential changes from $0.01a_{ho}$ to $0.02a_{ho}$. This comparatively large dependence on R_0 indicates that the properties of the system with two heavy atoms and one light atom are not fully determined by the s -wave scattering length for the ranges considered. In the $R_0 \rightarrow 0$ limit, the $\kappa = 4$ system is expected to behave universal [23, 27]. We speculate that the comparatively strong dependence of the normalized energy curve on the range for $a_s > 0$ is related to the fact that the three-particle system supports, for sufficiently large

κ , bound states with negative energy.

For comparison, circles and crosses in Fig. 4 show selected three-particle energies calculated by the FN-DMC method for $L = 0$ and $L = 1$, respectively. The good agreement with the CG results (lines) indicates that the FN-DMC method can be used to accurately describe different symmetry states.

Our CG energies for equal-mass systems interacting through short-range potentials presented in Fig. 4(a) can be compared with those of Kestner and Duan [31] obtained for zero-range interactions. Our $L = 1$ energy curve agrees with that of Kestner and Duan for all scattering lengths a_s considered. The $L = 0$ energy curve, however, only agrees for $a_s < 0$. For $a_s > 0$, our results are noticeably lower than those of Kestner and Duan. As shown below, our $a_s > 0$ results for $L = 0$ predict the correct atom-dimer scattering length suggesting that our energies should be very close to those for $R_0 = 0$ and that the disagreement is not due to finite-range effects. We speculate that the results of Kestner and Duan might not be fully converged for $a_s > 0$ although other possibilities cannot be excluded.

Figures 5(a) and (b) present the BCS and BEC limiting behaviors for an equal mass system with $N = 3$. The perturbative expression, Eq. (15), on the BEC side is expected to be applicable if $R_0 \ll a_s \ll a_{ho}$; thus, we choose a small R_0 , i.e., $R_0 = 0.005a_{ho}$, in the CG calculations. The energy is in this region determined by the atom-dimer scattering length a_{ad} [see Eq. (15)]. The CG energies change linearly with a_s , showing that a_{ad} is proportional to a_s , i.e., $a_{ad} = c_{ad}a_s$. A simple linear fit to the CG results predicts $c_{ad} \approx 1.21$, in good agreement with previous studies [71, 72], which found $a_{ad} \approx 1.2a_s$. A solid line in Fig. 5(a) shows the resulting linear expression. A more sophisticated analysis accounts for the energy-dependence of a_{ad} [73, 74], which results in a more reliable determination of c_{ad} and also a determination of the effective range r_{ad} [21]. Considering the three lowest energy levels on the BEC side [21], we obtain $c_{ad} \approx 1.18(1)$ and $r_{ad} \approx 0.08(1)a_s$. It was suggested earlier [24] that the atom-dimer system is characterized by a soft-core repulsion with range of the order of a_s ; our calculations support this general picture but predict a range about ten times smaller than a_s . On the BCS side, the first order correction varies also linearly with a_s . Circles in Fig. 5(b) show the CG results while the solid line shows the prediction from Eq. (13). Good agreement is observed in both limiting behaviors.

Our CG energies for $N = 2, 3$ and 4 can be readily combined to determine the excitation gap $\Delta(3)$, Eq. (21). Figure 6 shows the excitation gap $\Delta(3)$ as a function of a_{ho}/a_s for two different mass ratios, i.e., $\kappa = 1$ and 4. In the weakly-interacting molecular BEC regime, the excitation gap approaches $3\hbar\omega/2 - E(1,1)/2$ (circles), independent of the mass ratio. In the weakly-interacting BCS regime, however, the excitation gap depends on the mass ratio (see inset of Fig. 6). For equal masses, $\Delta(3)$ is very well described by the perturbative expression for

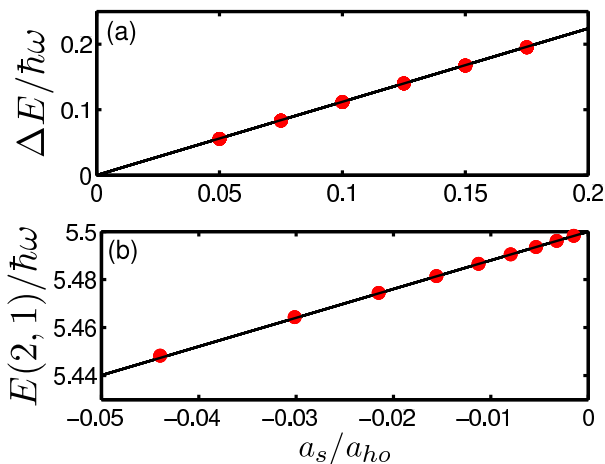


FIG. 5: (Color Online) Limiting behavior of the ground state energy for $N = 3$ equal mass fermions. (a) Energy correction $\Delta E = E(2,1) - E(1,1) - 3\hbar\omega/2$ on the BEC side. Circles show the CG results while the solid line shows the first order correction for $a_{ad} \approx 1.2a_s$. (b) Energy $E(2,1)$ on the BCS side. Circles show the CG results while the solid line shows the first order correction on the BCS side.

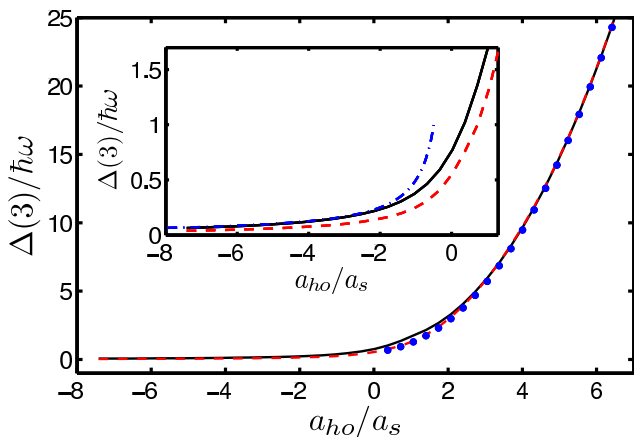


FIG. 6: (Color Online) Excitation gap $\Delta(N)$ for $N = 3$ as a function of a_{ho}/a_s calculated by the CG approach for $\kappa = 1$ (solid line) and $\kappa = 4$ (dashed line). Circles present the BEC limiting behavior $3\hbar\omega/2 - E(1,1)/2$ which is independent of κ . The inset shows a blow-up of the region where $\Delta(3)$ is smallest; in this region, the dependence of $\Delta(3)$ on κ is most pronounced. The dash-dotted line shows the limiting behavior for $\kappa = 1$ obtained by approximating the $E(N)$ in Eq. (21) by their perturbative values, Eq. (13).

$a_s \lesssim -0.5a_{ho}$ (dash-dotted line in the inset). Figure 6 shows that $\Delta(3)$ is smaller for $\kappa = 4$ than for $\kappa = 1$. Intuitively, this might be expected since the radial densities of the two species do not fully overlap for unequal masses (recall, we consider the case where species one and two experience the same trapping frequency). Thus, the pairing mechanism is expected to be less efficient in the unequal-mass system, especially on the BCS side, than in the equal-mass system. The next section discusses the

TABLE III: CG and FN-DMC energies E at unitarity for small equal-mass systems with angular momentum $L = 0$ and 1. The CG energies are calculated for the Gaussian interaction potential with $R_0 = 0.01a_{ho}$ for $N = 3$ and 4, and with $R_0 = 0.05a_{ho}$ for $N = 5$ and 6. The FN-DMC energies are calculated for the square well interaction potential with $R_0 = 0.01a_{ho}$. The guiding functions ψ_{T1} and ψ_{T2} , Eqs. (35) and (40), are used to obtain the energies of states with $L = 0$ and 1, respectively.

N	L	$E/(\hbar\omega)$ (CG)	$E/(\hbar\omega)$ (FN-DMC)
3	0	4.682	4.67(3)
3	1	4.275	4.281(4)
4	0	5.028	5.051(9)
5	0	8.03	8.10(3)
5	1	7.53	7.61(1)
6	0	8.48	8.64(3)
7	0		11.85(5)
7	1		11.36(2)
8	0		12.58(3)
9	0		15.84(6)
9	1		15.69(1)

behavior of the excitation gap at unitarity in more detail.

B. Ground state energy at unitarity

This section explores the odd-even behavior of two-component Fermi gases at unitarity. In particular, we present the excitation gap for equal-mass systems with up to $N = 30$ fermions and interpret the behaviors of these systems within the hyperspherical framework. We also discuss the excitation gap for small unequal-mass systems.

Table III summarizes selected CG and FN-DMC energies for small equal-mass systems at unitarity. Some of these energies were already reported in Refs. [20, 21], and we include them in Table III for comparative purposes. A comparison of the CG and FN-DMC energies for $N \leq 6$ shows that the FN-DMC energies agree to within 2% with the CG energies for both $L = 0$ and 1 states. This agreement suggests that the nodal surface used in the FN-DMC calculations is quite accurate. Thus, Table III shows that the FN-DMC method allows not only for an accurate description of the ground state but also of excited states. For $N = 9$, the energy of the $L = 1$ state is by only about $0.15\hbar\omega$ smaller than that of the $L = 0$ state. The ground state energies for larger N are reported in Table II of Ref. [20]. For both even and odd N ($N > 9$), we find that the angular momentum of the lowest energy state at unitarity is zero. Our FN-DMC energies thus suggest that the total angular momentum of the lowest energy states at unitarity has $L = 1$ for small odd N systems and $L = 0$ for larger odd N systems. We note that this conclusion depends cru-

cially on the construction of the nodal surface entering the FN-DMC calculations. For $N = 19$, e.g., the energies at unitarity for $L = 2$ and 1 are less than $0.8\hbar\omega$ higher than the $L = 0$ energy; thus, the definite determination of the ordering of the states at unitarity with different angular momenta remains a challenge for odd- N systems with $N > 9$.

For homogeneous systems, the ground state energy per particle at unitarity E_u is related to the energy per particle E_{FG} of the non-interacting system by a universal proportionality constant ξ , $E_u = \xi E_{FG}$ [35, 37, 64]. Applying this result to the trapped unitary system with even N through the LDA, the ground state energy $E_{00}(N)$ of the trapped system becomes directly proportional to the energy E_{NI} of the non-interacting trapped system [21],

$$E_{00}(N) = \sqrt{\xi} E_{NI}. \quad (42)$$

An analysis of our FN-DMC energies for $N = 2 - 30$ suggests that the trapped unitary system shows little shell structure. This motivates us to “smooth” the non-interacting energies, i.e., we approximate E_{NI} by the extended Thomas-Fermi expression [75],

$$E_{NI,ETF} = \hbar\omega \frac{1}{4} (3N)^{4/3} \left(1 + \frac{1}{2} (3N)^{-2/3} \right). \quad (43)$$

To determine the proportionality constant ξ , we fit our even N energies for $N = 2 - 30$ to the expression $\sqrt{\xi_{tr}} E_{NI,ETF}$. We find $\xi_{tr} = 0.467$, and denote the resulting energies by E_{fit} . This value is in very good agreement with our previous result, $\xi_{tr} = 0.465$, obtained by including the energies for $N = 2 - 20$ only [21]. Circles in Fig. 7 show the residual energy $E_{00}(N) - E_{fit}$ for both even and odd N . For even N , the energy difference $E_{00}(N) - E_{fit}$ is at most $0.15\hbar\omega$ (except for $N = 30$, for which the error bar is large). This suggests that the energies of the trapped unitary system are indeed quite well described by $\sqrt{\xi_{tr}} E_{NI,ETF}$; in other words, our energies show little residual shell structure. As expected, the odd N energies are not even quantitatively described correctly by $E_{00}(N) - E_{fit}$. Instead, Fig. 7 shows that the residual energy $E_{00}(N) - E_{fit}$ for odd N (circles) agrees quite well with the excitation gap $\Delta(N)$ (squares). For comparison, triangles in Fig. 7 show the excitation gap calculated using DFT [76]. The good agreement between the DFT and FN-DMC results is encouraging.

The ground-state energies $E_{00}(N)$ determine the coefficients s_0 [see Eq. (27)] of the hyperradial potential $V_{s_0}(R)$ [see Eq. (26)]. Figures 8(a) and (b) show the lowest hyperradial potential curves $V(R)$ [$V(R) = V_{s_0}(R) + V_{trap}(R)$, where $V_{trap}(R) = \frac{1}{2}\mu_N\omega^2 R^2$ and $\mu_N = m$] for $N = 3 - 20$ in the non-interacting limit and at unitarity, respectively. The small R behavior of $V(R)$ is dominated by $V_{s_0}(R)$ while the large R behavior of $V(R)$ is dominated by $V_{trap}(R)$. Comparison of Figs. 8(a) and (b) shows that the attractive interactions lead to a lowering of the potential curves at unitarity compared to those of the non-interacting system. Furthermore, the

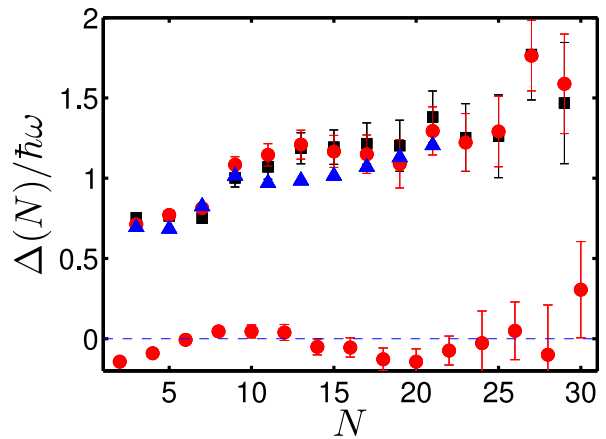


FIG. 7: (Color Online) Excitation gap $\Delta(N)$ (squares) and residual energy $E_{00}(N) - E_{fit}$ (circles) for equal-mass Fermi systems at unitarity as a function of N calculated from the FN-DMC energies. Triangles show $\Delta(N)$ calculated using density functional theory [76].

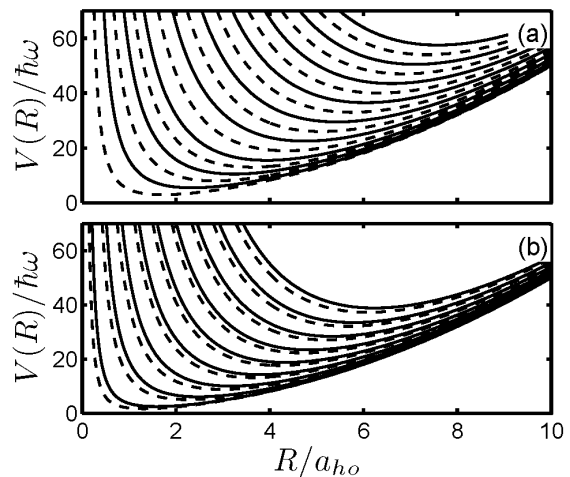


FIG. 8: Hyperradial potential curves $V(R)$ for equal-mass two-component Fermi systems with (a) vanishing interactions and (b) infinitely strong interactions as a function of R . The hyperradial potential curves naturally appear ordered as N increases: Solid lines correspond, from bottom to top, to $N = 4 - 20$ (N even), while dashed lines correspond, from bottom to top, to $N = 3 - 19$ (N odd).

$V(R)$ at unitarity appear “staggered”, i.e., odd-even oscillations are visible, reflecting the finite excitation gap at unitarity. In the non-interacting limit, in contrast, the excitation gap is zero and no odd-even staggering of the hyperradial potential curves is visible.

To extrapolate to the large N limit, Fig. 9 shows the normalized coefficients \bar{C}_N , Eq. (32) with E_{NI} replaced by $E_{NI,ETF}$, as a function of N (just as in our analysis of the energies E_{00} we find it useful to smooth the energies E_{NI}). The coefficients \bar{C}_N oscillate between two smooth curves, a curve for even N (circles) and a curve

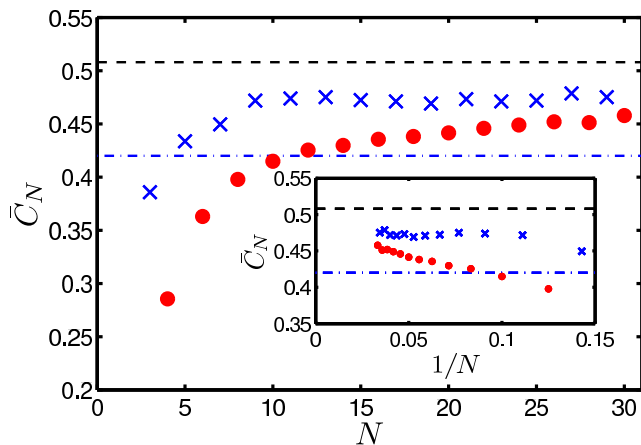


FIG. 9: (Color Online) Normalized coefficients \bar{C}_N , Eq. (32) with E_{NI} replaced by $E_{NI,ETF}$, as a function of N ; values for even N are shown by circles and values for odd N by crosses. The dash-dotted line shows the value $\xi = 0.42$ obtained by FN-DMC calculations for the homogeneous system [37, 64], while a dashed curve shows the value $\xi = 0.508$ obtained with a renormalization procedure [77]. The inset shows the same quantities as a function of $1/N$ instead of N .

for odd N (crosses). As N increases, the difference between the two curves decreases. In the large N -limit, the value of \bar{C}_N for two-component Fermi gases at unitarity should approach the universal parameter ξ [20]. This can be shown by relating the ground state energy obtained within the hyperspherical framework, Eq. (27), to the LDA prediction (see above), or by applying renormalized zero-range interactions within the hyperspherical framework [55]. The dash-dotted and dashed lines in Fig. 9 show the ξ value obtained by FN-DMC calculations for the homogeneous system ($\xi = 0.42$) [37, 64] and the ξ value obtained with a renormalization procedure ($\xi = 0.508$) [77], respectively. It is generally believed that the FN-DMC calculations provide the most reliable estimate for ξ to date. For comparison, our energies for the trapped system predict $\xi_{tr} = 0.467$ (see above). The circles in Fig. 9 approach this value. We attribute the fact that ξ_{tr} is larger than the corresponding value of the bulk system, i.e., $\xi = 0.42$, to the comparatively small system sizes ($N \leq 30$) included in our analysis. If this was true, we would expect the circles in the main part of Fig. 9 to turn around at larger N values. We note that we cannot rule out that the nodal surface entering our FN-DMC calculations might not be optimal.

In addition to equal-mass unitary systems, we study small systems with unequal masses at unitarity. Figure 10 shows the excitation gap $\Delta(N)$ for $N = 3$ at unitarity as a function of the mass ratio κ . $\Delta(3)$ decreases from about $0.8\hbar\omega$ for $\kappa = 1$ to about $0.3\hbar\omega$ for $\kappa = 8$. A decrease of the excitation gap as a function of κ has recently also been reported for the homogeneous unequal-mass system at unitarity [78]. To better understand the decrease of $\Delta(N)$ with increasing κ , triangles and squares

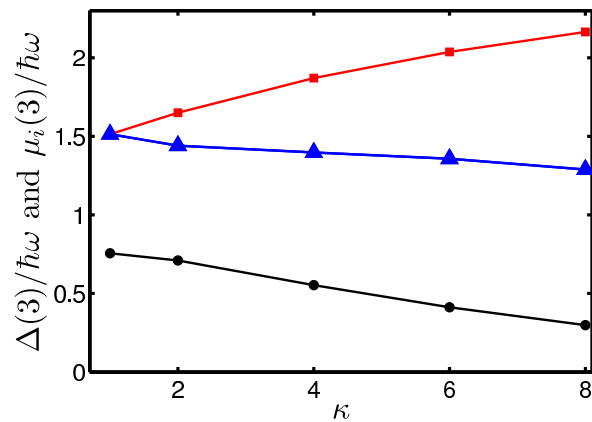


FIG. 10: (Color Online) Circles show the excitation gap $\Delta(N)$ for $N = 3$ as a function of the mass ratio κ at unitarity. Triangles and squares show the chemical potentials $\mu_1(3)$ and $\mu_2(3)$, respectively.

in Fig. 10 show the chemical potentials $\mu_1(3)$ and $\mu_2(3)$ for the two species. The decrease of μ_1 is related to the fact that trimers with negative energy form for sufficiently large κ . We additionally note that the densities of the light and heavy particles do not fully overlap. This effect is unique to the trapped system (the study of the homogeneous system with unequal masses [78] assumes equal densities of the two components and full pairing). Simple arguments lead one to conclude that a partial density overlap as opposed to a full density overlap leads to a decrease of the excitation gap. Thus, it is not clear if the decrease of $\Delta(3)$ visible in Fig. 10 with κ is due to the same mechanisms that lead to a decrease of Δ in the homogeneous system or due to the specifics of the trapping potentials, or possibly both.

C. Excitation spectrum at unitarity

Excitation spectra of two-component Fermi gases are rich. For four equal-mass fermions, e.g., Ref. [59] shows how the spectrum evolves from the non-interacting limit for small $|a_s|$, $a_s < 0$, to different families in the small a_s region, $a_s > 0$: One family consists of states that describe two bound dimers, another consists of states that describe a bound dimer plus two atoms, and yet another consists of states that describe a gas. Between these two limiting cases is the unitary region where the eigenspectrum is expected to be characterized by unique properties, similar to those of the non-interacting system (see Sec. II C). In particular, in the unitary regime families of eigenenergies separated by $2\hbar\omega$ are expected to exist [54]. This prediction has recently been verified for up to six particles with equal masses to within numerical accuracy, i.e., to within 2% [20]. Here we extend our analysis to unequal-mass systems with $N = 4$ and $L = 0$.

Circles in Fig. 11 show the zero angular-momentum energy spectrum calculated by the CG approach for four

particles at unitarity as a function of κ . The range of the Gaussian potential is $R_0 = 0.01a_{ho}$. To analyze the

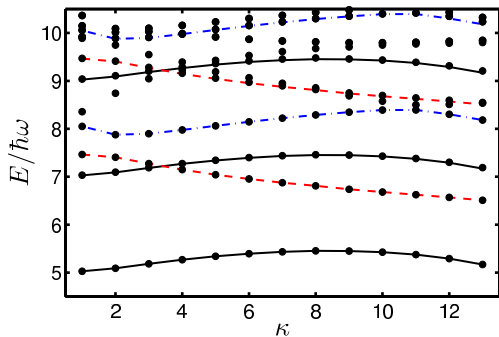


FIG. 11: (Color Online) Four-body energy spectrum for $L = 0$ at unitarity as a function of κ . Circles correspond to the numerical results obtained by the CG approach. Solid, dashed and dash-dotted lines show the energies $E_{\nu 0} + 2n\hbar\omega$ for $\nu = 0, 1$ and 2 , respectively ($n = 0, 1, \dots$).

eigenenergies, we employ the hyperspherical framework. Assuming that the separation of the wave function (see Sec. II C) holds for the short-range interactions considered here, we expect that the energy spectrum consists of families of energy levels separated by $2\hbar\omega$. Solid lines show the energies $E_{00} + 2n\hbar\omega$ (n non-negative integer), where E_{00} denotes the lowest positive energy of the spectrum (for sufficiently large κ , negative energy states form; these are not shown in Fig. 11). The agreement between the solid lines and the CG energies indicates that the $2\hbar\omega$ spacing, predicted for zero-range interactions, is fulfilled within our numerical accuracy. We repeat this exercise for the next family of energy levels: Dashed lines show the energy $E_{10} + 2n\hbar\omega$, where E_{10} corresponds to the lowest positive energy not yet assigned to a family. Similarly, dash-dotted lines connect states belonging to the third family. In addition to the just outlined assignment of quantum numbers, we checked in a few cases that the hyperradial wave functions $F_{\nu n}(R)$ corresponding to the energies $E_{\nu n}$ possess n hyperradial nodes (see also Sec. IV E). The lines in Fig. 11 show a crossing of energy levels belonging to different families at $\kappa \approx 4$. In close vicinity to this crossing, the spacing may not be exactly $2\hbar\omega$.

As already pointed out in the previous section, the energies $E_{\nu 0}$ determine the coefficients s_ν of the hyperradial potential curves $V_{s_\nu}(R)$. Table IV summarizes the three smallest coefficients for various κ . To the best of our knowledge, these are the first calculations of the s_ν for four-particle systems with unequal masses.

D. Structural properties along the BEC-BCS crossover

In addition to the energetics, we analyze the one-body densities and pair distribution functions of two-component Fermi systems in the crossover regime for dif-

TABLE IV: Coefficients s_ν of the hyperradial potential curves $V_{s_\nu}(R)$, Eq. (26), for the $N = 4$ system with $L = 0$ for various mass ratios κ .

κ	s_0	s_1	s_2	κ	s_0	s_1	s_2
1	2.03	4.46	5.05	8	2.45	3.81	5.29
2	2.09	4.41	4.88	9	2.45	3.74	5.35
3	2.18	4.27	4.90	10	2.42	3.68	5.39
4	2.27	4.15	4.98	11	2.37	3.62	5.39
5	2.34	4.04	5.06	12	2.29	3.57	5.30
6	2.40	3.95	5.15	13	2.17	3.51	5.18
7	2.43	3.88	5.22				

ferent κ . While the densities $\rho_i(\vec{r})$ of $L = 0$ states are spherically symmetric, those of states with $L > 0$ are not spherically symmetric. In the following, we determine the averaged radial densities $\rho_i(r)$, normalized so that $4\pi \int \rho_i(r)r^2 dr = N_i$; $4\pi r^2 \rho_i(r)/N_i$ tells one the probability of finding a particle with mass m_i at a distance r from the center of the trap. If $N_1 = N_2$ and $m_1 = m_2$, the radial one-body densities $\rho_1(r)$ and $\rho_2(r)$ coincide. If m_1 and m_2 or N_1 and N_2 differ, however, the radial one-body densities $\rho_1(r)$ and $\rho_2(r)$ are, in general, different. We also determine the averaged radial pair distribution functions $P_{ij}(r)$, normalized so that $4\pi \int P_{ij}(r)r^2 dr = 1$; $4\pi r^2 P_{ij}(r)$ tells one the probability to find a particle of mass m_i and a particle of mass m_j at a distance r from each other. For notational simplicity, we refer to the radial one-body densities as one-body densities and to the radial pair distribution functions as pair distribution functions in the following.

Figure 12 shows the pair distribution function $P_{12}(r)$ for $N = 3$ (dash and dash-dotted lines correspond to $L = 0$ and 1 , respectively) and $N = 4$ (solid lines) along the crossover for $\kappa = 1$. Panel (a) shows results for $a_s = -a_{ho}$, panel (b) for $1/a_s = 0$ and panel (c) for $a_s = 0.1a_{ho}$. Interestingly, the pair distribution functions for $N = 3$ and 4 show a similar overall behavior. In the BCS regime [Fig. 12(a)], the quantity $P_{12}(r)r^2$ shows a minimum at small r (for very small r , $P_{12}(r)r^2$ goes smoothly but steeply to zero; this rapid change of $P_{12}(r)r^2$ is hardly visible on the scale shown in Fig. 12). At unitarity [Fig. 12(b)], $P_{12}(r)r^2$ shows a maximum at small r and a second peak at larger r . In the BEC regime [Fig. 12(c)], the two-peak structure is notably more pronounced. The peak at small r indicates the formation of tightly-bound dimers (one dimer for $N = 3$ and two dimers for $N = 4$), while the peak between $1a_{ho}$ and $2a_{ho}$ is related to the presence of larger atom-atom distances set approximately by the atom-dimer distance for the three-body system and the dimer-dimer distance for the four-body system. This interpretation suggests that the three-particle system has one small and one large interspecies distance, and the four-particle system has two small and two large interspecies distances. Indeed, integrating $P_{12}(r)$ for $N = 3$ and 4 from 0 to the r

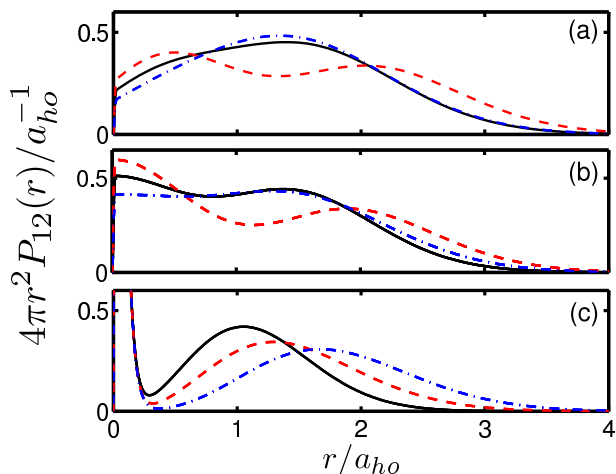


FIG. 12: (Color Online) Pair distribution functions $P_{12}(r)$, multiplied by r^2 , for equal mass two-component Fermi systems with $N = 3$ and $L = 0$ (dashed lines), $N = 3$ and $L = 1$ (dash-dotted lines), and $N = 4$ and $L = 0$ (solid lines) obtained by the CG approach for three different scattering lengths a_s : (a) $a_s = -a_{ho}$ (BCS regime), (b) $1/a_s = 0$ (unitarity), and (c) $a_s = 0.1a_{ho}$ (BEC regime). The pair distribution function for $N = 4$ and $a_s = 0.1a_{ho}$ [solid line in panel (c)] is shown in more detail in Fig. 13.

value at which $P_{12}(r)r^2$ exhibits the minimum, we find that the likelihood of being at small distances (forming a molecule) and being at large distances is the same.

We now analyze the pair distribution function $P_{12}(r)$ for $N = 4$ more quantitatively. Dash-dotted lines in Figs. 13(a) and (b) show the pair distribution function $P_{12}(r)$, multiplied by r^2 , for two trapped atoms with $a_s = 0.1a_{ho}$ (normalized to 1/2). This dimer curve is essentially indistinguishable from the small r part of the four-particle pair distribution function (circles). To describe the large r part of the four-particle pair distribution function, we consider two bosonic molecules of mass $2m$, which interact through an effective repulsive potential with dimer-dimer scattering length $a_{dd} \approx 0.6a_s$ [21, 23]. The dashed line in Fig. 13(a) shows the pair distribution function for this system under external confinement. This dashed curve is essentially indistinguishable from the large r part of the pair distribution function for the four-particle system. For comparison, a dotted line shows the pair distribution function for two non-interacting trapped bosons of mass $2m$. Figure 13 indicates that the effective repulsive interaction between the two dimers is crucial for reproducing the structural properties of the four-body system accurately. Our analysis shows that the entire pair distribution function $P_{12}(r)$ of the four-body system in the weakly-interacting molecular BEC regime can be described quantitatively in terms of a “dimer picture”.

We now return to Fig. 12 and discuss how the symmetry-inversion of the $N = 3$ system along the crossover (see Sec. IV A) is reflected in $P_{12}(r)$. In the BCS regime and at unitarity [Figs. 12(a) and (b)], $P_{12}(r)$

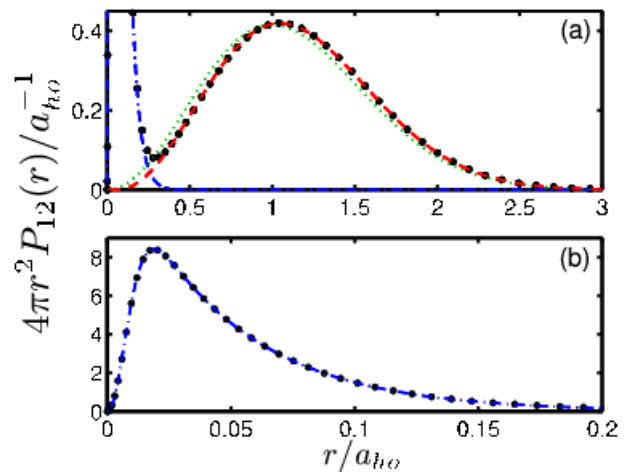


FIG. 13: (Color Online) (a) Circles show the pair distribution function $P_{12}(r)$, multiplied by r^2 , for $a_s = 0.1a_{ho}$ (BEC regime) calculated by the CG approach for $N = 4$ and $\kappa = 1$ [note, this quantity is also shown by a solid line in Fig. 12(c)]. For comparison, the dash-dotted line (blue online) shows $P_{12}(r)r^2$ for two atoms of mass m with the same scattering length but normalized to 1/2, the dashed line (red online) shows $P_{12}(r)r^2$ for two trapped bosonic molecules of mass $2m$ interacting through a repulsive effective potential with $a_{dd} = 0.6a_s$, and the dotted line (green online) shows $P_{12}(r)r^2$ for two trapped non-interacting bosonic molecules of mass $2m$. Panel (b) shows a blow-up of the small r region.

shows less structure for $L = 1$ than for $L = 0$. In the weakly-interacting molecular BEC regime [Fig. 12(c)], the pair distribution function for $L = 0$ nearly coincides with that for $L = 1$ at small r but is more compact than that for $L = 1$ at large r .

Next, we analyze how the behaviors of the pair distribution functions $P_{12}(r)$ for $N = 3$ and 4 change along the crossover if the mass ratio is changed from $\kappa = 1$ to 4. Figure 14 shows the pair distribution functions for $\kappa = 4$. For $N = 3$, we consider three-particle systems with either a spare light particle or with a spare heavy particle. The pair distributions for the three-particle system with two light particles and one heavy particle are notably broader than those for the three-particle system with one light particle and two heavy particles. This behavior can be attributed to the fact that $a_{ho}^{(1)} > a_{ho}^{(2)}$. Besides this, a comparison of the pair distribution functions shown in Fig. 14 for $\kappa = 4$ and those shown in Fig. 12 for $\kappa = 1$ reveals that the overall behavior of the $P_{12}(r)$ is similar.

Figures 15(a) and (b) show the one-body densities for $\kappa = 1$ and 4, respectively. In the non-interacting limit [the solid lines show $\rho_1(r)$ and the circles show $\rho_2(r)$], the sizes of $\rho_1(r)$ and $\rho_2(r)$ are determined by $a_{ho}^{(1)}$ and $a_{ho}^{(2)}$, respectively. As is evident in Fig. 15, the density of the light particles extends to larger r than the density of the heavy particles. The density mismatch for $\kappa = 4$ between the two one-body densities decreases as a_s is tuned through the strongly-interacting regime to the

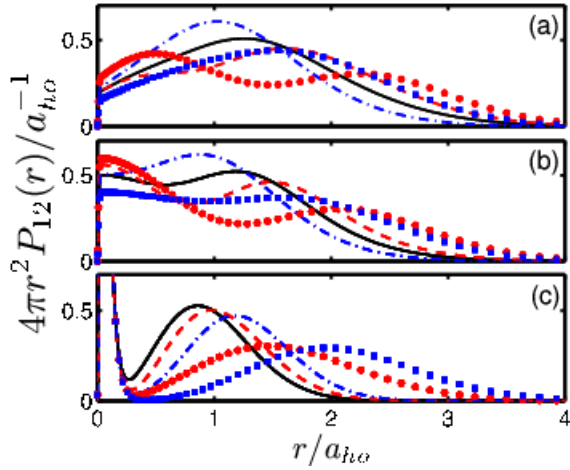


FIG. 14: (Color Online) Pair distribution function $P_{12}(r)$, multiplied by r^2 , for two-component Fermi gases with $\kappa = 4$ for different scattering lengths a_s : (a) $a_s = -a_{ho}$ (BCS regime), (b) $1/a_s = 0$ (unitarity), and (c) $a_s = 0.1a_{ho}$ (BEC regime). Dashed and dash-dotted lines show $P_{12}(r)r^2$ for $N = 3$ (two heavy particles) with $L = 0$ and 1 , respectively. Circles and squares show $P_{12}(r)r^2$ for $N = 3$ (two light particles) with $L = 0$ and 1 , respectively. Solid lines show $P_{12}(r)r^2$ for $N = 4$ with $L = 0$.

weakly-interacting molecular BEC side. In the weakly-interacting molecular BEC regime, two molecules consisting each of a heavy and a light particle form. In this regime, the size of the system is determined by the molecular trap length and the densities $\rho_1(r)$ and $\rho_2(r)$ [triangles and dash-dotted line in Fig. 15(b)] nearly coincide. Furthermore, the densities are to a very good approximation described by the one-body density for two bosonic molecules of mass $m_1 + m_2$ interacting through an effective repulsive interaction characterized by the dimer-dimer scattering length ($a_{dd} \approx 0.77a_s$ for $\kappa = 4$ [21, 23]).

We have also analyzed the pair distribution functions $P_{ii}(r)$ for $\kappa = 1$ and 4 (not shown). The small r region of the $P_{ii}(r)$ is controlled by the Pauli exclusion principle between identical fermions. In the weakly-interacting molecular BEC regime, the pair distribution functions $P_{11}(r)$ and $P_{22}(r)$ nearly coincide even for $\kappa = 4$. In this regime, the pair distribution functions $P_{ii}(r)$ are well approximated by that for two particles of mass $m_1 + m_2$ interacting with a repulsive potential characterized by a_{dd} .

E. Structural properties at unitarity

This section discusses selected structural properties of two-component equal mass Fermi gases at unitarity with up to $N = 20$ atoms. For small systems ($N \leq 6$), we present structural properties calculated using both the CG and the FN-DMC methods. For larger systems, however, our interpretation relies solely on the structural properties calculated by the FN-DMC method.

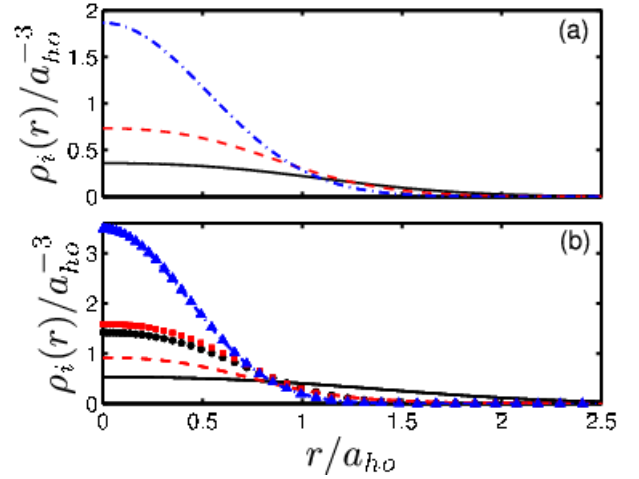


FIG. 15: (Color Online) One-body densities $\rho_1(r)$ and $\rho_2(r)$ for $N = 4$ and (a) $\kappa = 1$ and (b) $\kappa = 4$ for different scattering lengths a_s [for $\kappa = 1$, $\rho_1(r)$ and $\rho_2(r)$ coincide and only $\rho_2(r)$ is shown]: Circles and solid lines show $\rho_1(r)$ and $\rho_2(r)$ for $a_s = 0$, squares and dashed lines show $\rho_1(r)$ and $\rho_2(r)$ for $1/a_s = 0$, and triangles and dash-dotted lines show $\rho_1(r)$ and $\rho_2(r)$ for $a_s = 0.1a_{ho}$. Note, $\rho_2(r)$ for $\kappa = 4$ and $a_s = 0$ [solid line in panel (b)] is multiplied by a factor of three to enhance the visibility.

To assess the accuracy of the nodal surfaces employed in our FN-DMC calculations as well as of the accuracy of the mixed estimator [see Eq. (41) in Sec. III B], Figs. 16(a) and (b) compare the pair distribution functions $P_{12}(r)$ for the three-particle system with $L = 1$ and the four-particle system with $L = 0$, respectively, calculated by the CG and the FN-DMC methods. The

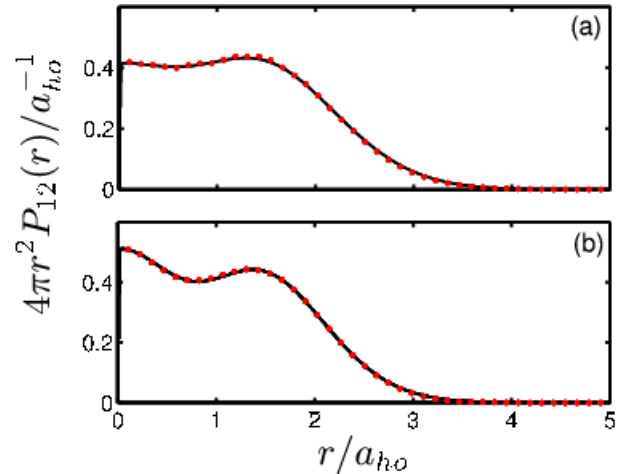


FIG. 16: (Color Online) Pair distribution functions $P_{12}(r)$, multiplied by r^2 , at unitarity for equal mass Fermi systems with (a) $N = 3$ ($L = 1$) and (b) $N = 4$ ($L = 0$) atoms calculated by the CG method (solid lines) and by the FN-DMC method (circles). The agreement is excellent.

agreement between the pair distribution functions calculated by the CG method (solid lines) and the FN-DMC

method (circles) is very good, validating the construction of the nodal surface of ψ_T . Furthermore, the good agreement suggests that the mixed estimator results, for the guiding functions employed, in structural properties very close to those one would obtain by an exact estimator.

Figure 17 shows the pair distribution functions $P_{12}(r)$ calculated by the FN-DMC method for equal mass Fermi systems with $N = 3 - 20$ at unitarity. To simplify the

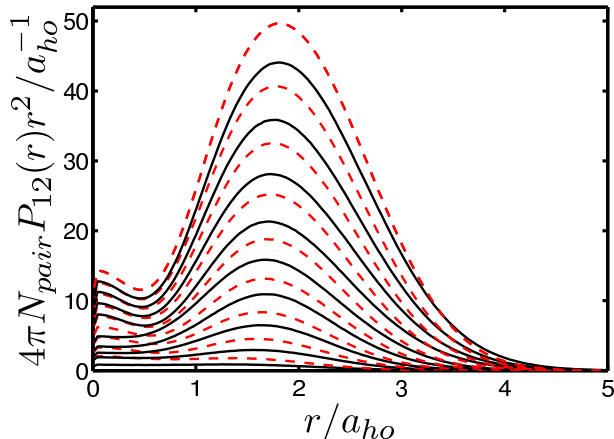


FIG. 17: (Color Online) Dashed and solid lines show the pair distribution functions $P_{12}(r)$, multiplied by $r^2 N_{pair}$ (N_{pair} denotes the number of interspecies distances), for equal mass Fermi systems at unitarity with even N ($N = 4, 6, \dots, 20$) and odd N ($N = 3, 5, \dots, 19$), respectively, calculated by the FN-DMC. Beyond $r \approx a_{ho}$, $P_{12}(r)r^2 N_{pair}$ is smallest for $N = 3$ and largest for $N = 20$.

comparison, Fig. 17 shows the even N results as a dashed line and the odd N results as a solid line. Furthermore, $P_{12}(r)r^2$ is multiplied by the number N_{pair} of interspecies distances so that the $N = 3$ distribution function has the smallest and the $N = 20$ distribution function the largest amplitude for $r \gtrsim a_{ho}$. The pair distribution functions for even N show a similar behavior for all N considered; both the small r and the large r peaks grow monotonically and smoothly with increasing N . For odd N , in contrast, the small r peak changes somewhat discontinuously at $N \approx 11$. This behavior can be attributed to the guiding functions employed. For even N , the guiding function ψ_{T1} , whose nodal surface is constructed from the two-body solution, gives the lowest energy for all N (except for $N = 4$). For odd N , however, ψ_{T2} results in a lower energy for $N \leq 9$, ψ_{T3} for $N = 11$, and ψ_{T1} for $N \geq 13$. Thus, the pair distribution functions clearly reveal how the structural properties depend on the nodal surface employed in the FN-DMC calculations and provide much deeper insights into the different ψ_T employed than a mere comparison of the energies.

For $N \geq 13$, Fig. 17 indicates that the amplitudes of the scaled interspecies pair distribution functions are nearly the same for neighboring systems. For example, the quantities $P_{12}(r)r^2 N_{pair}$ for $N = 18$ and 19 agree to a good approximation, suggesting that one can think

of the $N = 18$ system as consisting of nine pairs, and of the $N = 19$ system as consisting of nine pairs plus a spare atom. Note that this interpretation hinges critically on the nodal surface employed in our FN-DMC calculations; a small change in the nodal structure of the guiding function may change the small r behavior of the pair distribution functions non-negligibly.

We next investigate in Fig. 18 where the spare particle is located in the odd- N systems at unitarity. This fig-

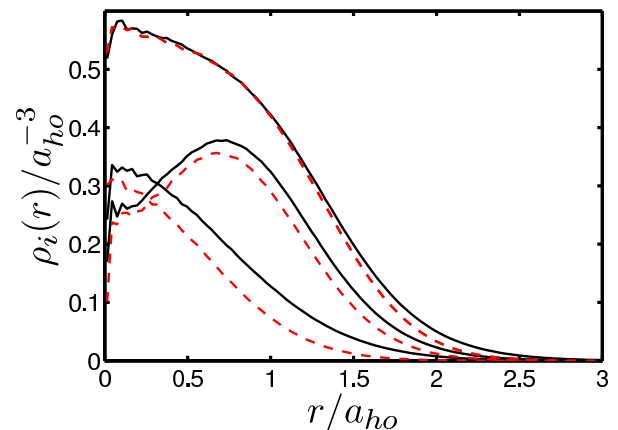


FIG. 18: (Color Online) The one-body density $\rho_1(r)$ (solid lines) is shown for $N = 3, 9$ and 15 (for $r > 0.5a_{ho}$, from bottom to top), together with the one-body density $\rho_2(r)$ (dashed line) for $N = 3, 9$ and 15 (for $r > 0.5a_{ho}$, from bottom to top) for equal mass two-component Fermi gases at unitarity calculated by the FN-DMC method.

ure shows the one-body densities $\rho_1(r)$ (solid lines) and $\rho_2(r)$ (dashed lines) for $N = 3, 9$ and 15 . For $N = 3$, the difference between $\rho_1(r)$ and $\rho_2(r)$ is roughly constant across the trap. The behavior is similar for $N = 9$. Interestingly, the densities for $N = 9$ show a minimum at $r = 0$, reflecting the fact that the FN-DMC calculations employ the nodal surface of the ideal Fermi gas, i.e., use ψ_{T2} [Eq. (40)]. For $N = 15$, the nodal surface employed is constructed from the two-body solution [see Eq. (35)], and consequently, the behavior of the density profiles differs from that for the smaller N . The densities $\rho_1(r)$ and $\rho_2(r)$ nearly coincide at small r . At large r , however, the density $\rho_1(r)$ has a larger amplitude than $\rho_2(r)$ (recall $N_1 = N_2 + 1$). Our data for $N = 15$ indicate that the spare particle is not distributed uniformly throughout the trap but has an increased probability to be found near the edge of the cloud. Possible consequences of this finding for the excitation gap have already been discussed in Refs. [20, 79].

To quantify the analysis of the one-body densities, we integrate $\rho_i(r)$ over r ,

$$\bar{N}_i(r) = 4\pi \int_0^r \rho_i(r') r'^2 dr'. \quad (44)$$

For a finite upper integration limit, $\bar{N}_i(r)$ monitors how many of the \bar{N}_i particles are located between zero and

r . Figure 19 shows $\bar{N}_i(r)$ for $N = 3, 9$ and 15 . As in Fig. 18, the results for component one are shown by solid lines and those for component two by dashed lines; in the large r limit, the $\bar{N}_i(r)$ equal N_i , as expected. One can now read off nicely, in which r -regions the densities of

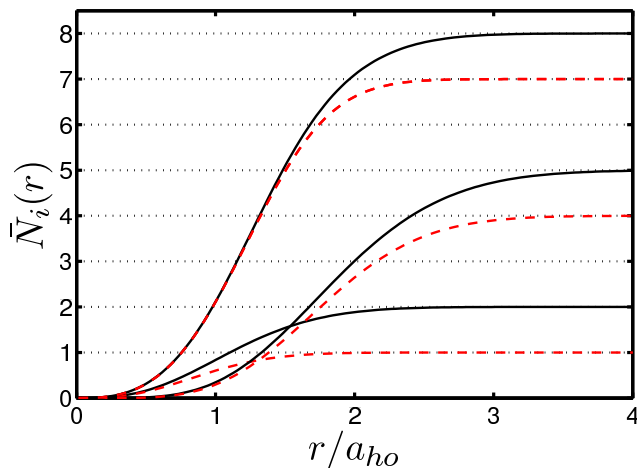


FIG. 19: (Color Online) Solid and dashed lines show the integrated quantities $\bar{N}_1(r)$ and $\bar{N}_2(r)$ [Eq. (44)], respectively, as a function of r for a two-component Fermi gas at unitarity. At large r , the curves correspond from bottom to top to $N = 3, 9$ and 15 .

the two components agree and where they disagree. For $N = 3$, e.g., the two atoms of component one and the one atom of component two are added over approximately the same r -region. For $N = 15$, in contrast, the first five atoms of the two components are located in the region with $r \lesssim 1.5a_{ho}$; this core region can be considered “fully paired”. The last three atoms of component one and the last two atoms of component two form, loosely speaking, a “partially paired or unpaired outer shell”. We find similar behaviors for the odd- N systems with $N = 13, 17$ and 19 . It will be interesting to see if this interpretation holds for larger N , and if this information can be used to shed light on the phase diagram of asymmetric Fermi gases [80, 81].

To further verify the validity of the special properties of two-component Fermi gases at unitarity as well as to further assess the accuracy of our guiding functions employed in the FN-DMC calculations, we analyze the hyperradial densities $\bar{F}_{00}^2(x)$ for various N . Symbols in Fig. 20 show the dimensionless hyperradial density $\bar{F}_{00}^2(x)$ calculated using the mixed Monte Carlo estimator, Eq. (41), for $N = 3$ to 10 . Here, x is the dimensionless hyperradius defined just above Eq. (30) and the normalization of the \bar{F}_{00} is chosen so that $\int_0^\infty \bar{F}_{00}^2(x) dx = 1$. The dimensionless hyperradius x is scaled by R'_{NI} , which we evaluate by approximating E_{NI} in Eq. (31) by $E_{NI,EFT}$. This is similar to the “smoothing procedure” discussed in the context of Figs. 7 and 9. The hyperradial densities become more compact as N increases, owing to the increase of the effective mass μ_{eff} entering into the

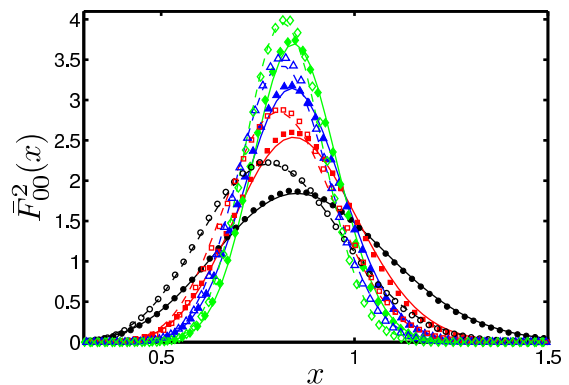


FIG. 20: (Color Online) The hyperradial density $\bar{F}_{00}^2(x)$ is shown as a function of the dimensionless hyperradius x for $N = 3 - 10$, calculated using the mixed Monte Carlo estimator (symbols) and the analytical expression with the FN-DMC energies (lines), respectively. The maximum of $\bar{F}_{00}^2(x)$ is smallest for $N = 3$ and largest for $N = 10$; the MC results are shown by filled circles for $N = 3$, open circles for $N = 4$, filled squares for $N = 5$, open squares for $N = 6$, filled triangles for $N = 7$, open triangles for $N = 8$, filled diamonds for $N = 9$ and open diamonds for $N = 10$.

effective hyperradial Schrödinger equation [Eq. (30)] with increasing N . Furthermore, the maximum of the hyperradial densities occurs at slightly larger x values for odd N systems than for even N systems, in agreement with the odd-even staggering discussed in Sec. IV B in the context of the hyperradial potential curves $V(R)$.

In the limit of zero-range interactions, the adiabatic approximation is expected to be exact (see Sec. II C). In this case, the functional form of the hyperradial wave functions is known analytically [see Eq. (28)], and can be compared with the Monte Carlo results obtained for short-range potentials by sampling the total wave function and integrating over all coordinates but the hyperradius. Solid lines in Fig. 20 show the hyperradial densities $\bar{F}_{00}^2(x)$ for $N = 3$ to 10 predicted analytically for zero-range interactions, using the FN-DMC energies E_{00} listed in Table III of this paper and Table II of Ref. [21]. The agreement between the analytical results and the Monte Carlo results obtained for finite range potentials is quite good. On the one hand, this agreement lends numerical support for the separability or near separability of the total wave function into a hyperradial and a hyperangular part. On the other hand, the good agreement suggests that the nodal surface employed in our MC calculations is appropriate.

Finally, we analyze the hyperradial densities calculated by the CG approach for the $N = 6$ system. Since the CG approach allows for the determination of excited states, this analysis allows us to verify that the $2\hbar\omega$ spacing reported in Ref. [20] and discussed in Sec. II C corresponds indeed to breathing-mode excitations, i.e., to excitations along the hyperradial coordinate. To extract the hyperradial densities, we integrate the square of the wavefunction Ψ^{rel} over all the coordinates but the hyperradius. If

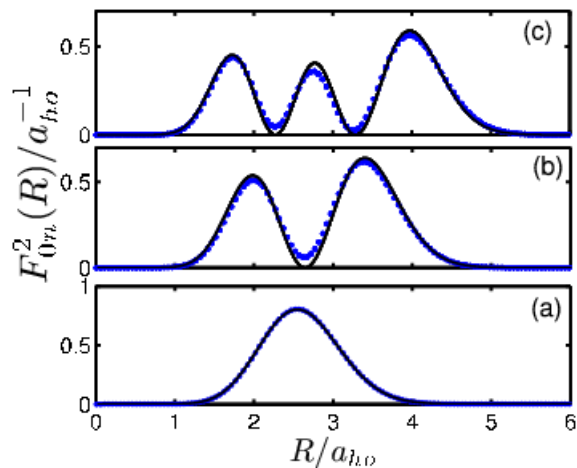


FIG. 21: (Color Online) Hyperradial density $F_{0\nu}^2(R)$ for $n = 1, 2$ and 3 . Here, we choose $\mu_N = m$ ($\mathcal{L} = a_{ho}$). The solid lines show the analytical solutions while the circles show the numerical results obtained by integrating $(\Psi^{rel})^2$ calculated by the CG method over all coordinates but the hyperradius R .

the universal behavior is fulfilled, then the hyperradial densities should coincide with the square of the analytically determined $F_{\nu n}(R)$, Eq. (28), which are shown in Fig. 21 by solid lines. The integration over the hyperangular coordinates is carried out using Monte Carlo integration techniques. Symbols in Fig. 21 show the resulting hyperradial densities $F_{\nu n}^2(R)$ for $\nu = 0$ and $n = 0, 1$ and 2 . The numerically determined hyperradial densities indicate that the excitations are to a good approximation located along the R coordinate, supporting the interpretation of the $2\hbar\omega$ spacing within the hyperspherical framework. The agreement between the numerical and analytical results is excellent for the ground state [see Fig. 21(a)]. For the excited states with $n = 1$ and 2 , the small deviations between the numerical and analytical results may be due to finite range effects or not fully converged numerical results.

V. CONCLUSIONS

This paper presents a microscopic picture of the properties of ultracold two-component fermionic systems in a trap. Complementing previous studies [20, 21], we focus on the energetics of odd N systems, and the structural properties of both odd and even N systems.

For sufficiently few particles, we solve the Schrödinger equation for equal and unequal mass systems, starting from a model Hamiltonian with short-range interspecies s -wave interactions using the CG approach. This basis set expansion technique allows for the determination of the eigenspectrum and eigenstates with controlled accuracy throughout the BEC-BCS crossover. We find that the spectrum and the structural properties of small trapped two-component Fermi systems change qualita-

tively throughout the crossover regime.

An analysis of the energies of the $N = 3$ systems in the weakly-interacting BEC and BCS regimes allows us to determine the validity regime of the analytically determined perturbative expressions for small $|a_s|$. Furthermore, we find that the angular momentum of the $N = 3$ ground state changes from $L = 1$ in the weakly-attractive BCS regime to $L = 0$ in the weakly-repulsive BEC regime for all mass ratios considered. By additionally treating the $N = 2$ and 4 systems, we determine the excitation gap $\Delta(3)$ throughout the crossover region: For equal frequencies, the excitation gap decreases for all scattering lengths with increasing mass ratio. For $N = 4$ systems with $\kappa \leq 13$, we determine the $L = 0$ excitation spectrum at unitarity. The spectrum determines the s_ν coefficients of the hyperradial potential curves and also verifies within our numerical accuracy the $2\hbar\omega$ spacing prediction, which was derived analytically assuming universality [54]. We verified in a number of cases that the $2\hbar\omega$ spacing corresponds indeed to breathing-mode excitations.

Our analysis of the energetics is complemented by studies of the structural properties. For the four-particle system with equal and unequal masses, e.g., we show how the pair distribution functions in the $a_s > 0$ region (small a_s) can be described by a system of two molecules interacting through an effective dimer-dimer potential with positive dimer-dimer scattering length. A similar analysis was carried out for the $N = 3$ system and we verified that this system behaves as an interacting system of an atom and a dimer.

Our small N studies have implications for optical lattice experiments. Our results can be applied directly if each optical lattice site is approximately harmonic in the non-tunneling regime. In this context, Ref. [31] already pointed out, including the energies of the two- and three-particle system, that the occupation of optical lattice sites with three equal-mass atoms is unfavorable. To start with let us consider a system with two lattice sites and six atoms (three of each species). We imagine that the lattice sites are loaded by adiabatically turning up the barrier height between the two sites. It follows from our energies calculated for $N = 2$ through 4 , that the system ends up with unequally occupied lattice sites at the end of the ramp: For both equal and unequal masses, and for all scattering lengths, the energy of the two-site lattice is minimal if two atoms occupy one site and the other four atoms occupy the other site. This is simply a consequence of the fact that $\Delta(3)$ is positive throughout the crossover (note, the energy of the unequal mass system might be further lowered if we consider the formation of pentamers and sextamers with negative energies; these states are not included in our analysis). The arguments presented here for just two lattice sites generalize readily to lattices with multiple sites.

Instead of ramping up the barrier height adiabatically, we now imagine a fast non-adiabatic ramp. In this case, the likelihood of finding three atoms per lattice site at

the end of the ramp is finite. Since the excitation frequencies for two-, three- and four-particle systems are different, a “purification sweep” [15] can be used to then prepare a system with either three or no particles per site. These three-particle systems could be investigated spectroscopically (see, e.g., Sec. IV C for a discussion of the excitation spectrum of the four-particle system). Alternatively, one might ask whether it would be possible to measure the odd-even physics by adiabatically lowering the lattice barrier and monitoring the point at which tunneling sets in.

In addition to systems with equal numbers of atoms in the two species, we consider an optical lattice with twice as many heavy as light atoms. If the mass ratio is sufficiently large, trimers consisting of two heavy atoms and one light atom with negative energy can form at each lattice site, paving the way for spectroscopic studies of these delicate systems. Furthermore, by starting with a bound trimer in a deep lattice and then lowering the lattice height, a gas consisting of bound trimers can possibly be prepared.

To extend the studies of the energetics and structural properties to larger systems, we employed the FN-DMC technique. This approach determines the lowest energy of a state that has the same symmetry as a so-called guiding function and thus an upper bound to the exact eigenenergy. Detailed comparisons of the energies and the structural properties calculated by the CG and FN-DMC approaches benchmark the nodal surfaces employed for systems with $N \leq 6$. In the strongly-correlated unitary regime, e.g., the FN-DMC energies for equal-mass two-component Fermi systems agree with the CG energies to within 2%.

Our even N energies ($N \leq 30$) for equal-mass systems at unitarity show vanishingly small shell structure. Applying the local density approximation and approximating the non-interacting energies by the corresponding extended Thomas-Fermi expression, we find $\xi_{tr} = 0.467$, which is somewhat larger than the value of the homo-

geneous system, $\xi_{hom} = 0.42$. We note that the expression $\sqrt{\xi_{tr}} E_{NI,EFT}$ describes the equal-mass energies for $N \leq 30$ at unitarity very well; the small disagreement between ξ_{tr} and ξ_{hom} is most likely due to the small number of particles considered in the present work. Combining the even and odd N energies, we find that the excitation gap $\Delta(N)$ at unitarity increases with N . Also, the one-body densities and pair distribution functions at unitarity are studied for up to $N = 20$. For odd N with $N \gtrsim 11$, we observe that the extra “unpaired” particle is located predominantly near the edge of the cloud, in agreement with previous predictions [20, 79]. This suggests that the LDA cannot be applied to determine the excitation gap. Furthermore, we find that the hyperradial densities of the lowest gas-like state with $N \leq 10$ calculated for short-range interactions by the FN-DMC method agree with the analytically predicted ones, indicating that the lowest gas-like state does indeed behave universally. Selected hyperradial densities for larger N were already presented in Ref. [20].

The energies and structural properties for the equal-mass two-component Fermi systems at unitarity presented in this paper may serve as a benchmark for other calculations. Recently, e.g., a DFT treatment determined the energies for systems with up to $N = 20$ particles [76]. The good agreement between the FN-DMC energies and the DFT energies suggests that the functional employed in the DFT calculations captures the key physics. However, close inspection of the FN-DMC and DFT energies indicates that the agreement between the even N and odd N energies is not equally good. While this could be a consequence of the nodal surfaces employed in our FN-DMC calculations, it could alternatively indicate that the DFT treatment employed in Ref. [76] for odd N is not optimal. Thus, it is hoped that our results will prove helpful in assessing the accuracy of the DFT approach and other approaches.

We acknowledge support by the NSF, and fruitful discussions with J. D’Incao and S. Giorgini.

-
- [1] W. C. Stwalley, Phys. Rev. Lett. **37**, 1628 (1976).
 - [2] E. Tiesinga, B. J. Verhaar, and H. T. C. Stoof, Phys. Rev. A **47**, 4114 (1993).
 - [3] S. Inouye, M. R. Andrews, J. Stenger, H. J. Miesner, D. M. Stamper-Kurn, and W. Ketterle, Nature **392**, 151 (1998).
 - [4] S. L. Cornish, N. R. Claussen, J. L. Roberts, E. A. Cornell, and C. E. Wieman, Phys. Rev. Lett. **85**, 1795 (2000).
 - [5] M. Greiner, C. A. Regal, and D. S. Jin, Nature **426**, 537 (2003).
 - [6] M. W. Zwierlein, C. A. Stan, C. H. Schunck, S. M. F. Raupach, S. Gupta, Z. Hadzibabic, and W. Ketterle, Phys. Rev. Lett. **91**, 250401 (2003).
 - [7] T. Bourdel, J. Cubizolles, L. Khaykovich, K. M. F. Magalhaes, S. J. J. M. F. Kokkelmans, G. V. Shlyapnikov, and C. Salomon, Phys. Rev. Lett. **91**, 020402 (2003).
 - [8] K. E. Strecker, G. B. Partridge, and R. G. Hulet, Phys. Rev. Lett. **91**, 080406 (2003).
 - [9] J. Kinast, S. L. Hemmer, M. E. Gehm, A. Turlapov, and J. E. Thomas, Phys. Rev. Lett. **92**, 150402 (2004).
 - [10] J. T. Stewart, J. P. Gaebler, C. A. Regal, and D. S. Jin, Physical Review Letters **97**, 220406 (2006).
 - [11] S. Giorgini, L. P. Pitaevskii, and S. Stringari, cond-mat/0706.3360 (2007).
 - [12] M. Köhl, H. Moritz, T. Stöferle, K. Günter, and T. Esslinger, Phys. Rev. Lett. **94**, 080403 (2005).
 - [13] H. Moritz, T. Stöferle, K. Günter, M. Köhl, and T. Esslinger, Phys. Rev. Lett. **94**, 210401 (2005).
 - [14] T. Rom, T. Best, D. van Oosten, U. Schneider, S. Fölling, B. Paredes, and I. Bloch, Nature **444**, 733 (2006).
 - [15] G. Thalhammer, K. Winkler, F. Lang, S. Schmid, R. Grimm, and J. Hecker Denschlag, Phys. Rev. Lett. **96**, 050402 (2006).

- [16] W. A. de Heer, *Rev. Mod. Phys.* **65**, 611 (1993).
- [17] J. P. Toennies and A. F. Vilesov, *Angew. Chem. Int. Ed.* **43**, 2622 (2004).
- [18] K. Lee, J. Callaway, and S. Dhar, *Phys. Rev. B* **30**, 1724 (1984).
- [19] P. Sindzingre, M. L. Klein, and D. M. Ceperley, *Phys. Rev. Lett.* **63**, 1601 (1989).
- [20] D. Blume, J. von Stecher, and C. H. Greene, *Phys. Rev. Lett.* **99**, 233201 (2007).
- [21] J. von Stecher, C. H. Greene, and D. Blume, *Phys. Rev. A* **76**, 053613 (2007).
- [22] D. S. Petrov, C. Salomon, and G. V. Shlyapnikov, *Phys. Rev. Lett.* **93**, 090404 (2004).
- [23] D. S. Petrov, C. Salomon, and G. V. Shlyapnikov, *J. Phys. B* **38**, S645 (2005).
- [24] D. S. Petrov, C. Salomon, and G. V. Shlyapnikov, *Phys. Rev. A* **71**, 012708 (2005).
- [25] V. Efimov, *Yad. Fiz.* **12**, 1080 (1970) [*Sov. J. Nucl. Phys.* **12**, 589 (1971)].
- [26] V. N. Efimov, *Nucl. Phys. A* **210**, 157 (1973).
- [27] O. Kartavtsev and A. Malykh, *J. Phys. B* **40**, 1429 (2007).
- [28] R. Jáuregui, R. Paredes, and G. T. Sánchez, *Phys. Rev. A* **76**, 011604 (R) (2007).
- [29] J. Schneider and H. Wallis, *Phys. Rev. A* **57**, 1253 (1998).
- [30] E. Fermi, *Nuovo Cimento* **11**, 157 (1934).
- [31] J. P. Kestner and L.-M. Duan, *Phys. Rev. A* **76**, 033611 (2007).
- [32] I. Stetcu, B. R. Barrett, U. van Kolck, and J. P. Vary, *Phys. Rev. A* **76**, 063613 (2007).
- [33] D. M. Eagles, *Phys. Rev.* **186**, 456 (1969).
- [34] A. J. Leggett, in “Modern Trends in the Theory of Condensed Matter”, ed. by A. Pekalski J. Przystawa, Springer, Berlin (1980).
- [35] J. Carlson, S. Y. Chang, V. R. Pandharipande, and K. E. Schmidt, *Phys. Rev. Lett.* **91**, 050401 (2003).
- [36] S. Y. Chang, V. R. Pandharipande, J. Carlson, and K. E. Schmidt, *Phys. Rev. A* **70**, 043602 (2004).
- [37] J. Carlson and S. Reddy, *Phys. Rev. Lett.* **95**, 060401 (2005).
- [38] S.-T. Wu, C.-H. Pao, and S.-K. Yip, *Phys. Rev. B* **74**, 224504 (2006).
- [39] M. Iskin and C. A. R. Sá de Melo, *Phys. Rev. Lett.* **96**, 040402 (2006).
- [40] G.-D. Lin, W. Yi, and L.-M. Duan, *Phys. Rev. A* **74**, 031604(R) (2006).
- [41] M. Iskin and C. A. R. Sá de Melo, *cond-mat/0703258* (2007).
- [42] M. M. Parish, F. M. Marchetti, A. Lamacraft, and B. D. Simons, *Nature Phys.* **3**, 12 (2007).
- [43] P. Ring and P. Schuck, *The Nuclear Many-Body Problem* (Springer, New York, 1980).
- [44] T. Paananen, P. Törmä, and J.-P. Martikainen, *Phys. Rev. A* **75**, 023622 (2007).
- [45] L. M. Delves, *Nucl. Phys.* **9**, 391 (1959).
- [46] L. M. Delves, *Nucl. Phys.* **20**, 275 (1960).
- [47] J. Macek, *J. Phys. B* **1**, 831 (1968).
- [48] Y. F. Smirnov and K. V. Shitikova, *Sov. J. Part. Nucl.* **8**, 44 (1977).
- [49] X. Chapuisat, *Phys. Rev. A* **45**, 4277 (1992).
- [50] C. D. Lin, *Phys. Rep.* **257**, 1 (1995).
- [51] J. L. Bohn, B. D. Esry, and C. H. Greene, *Phys. Rev. A* **58**, 584 (1998).
- [52] S. T. Rittenhouse, M. J. Cavagnero, J. von Stecher, and C. H. Greene, *Phys. Rev. A* **74**, 053624 (2006).
- [53] O. Sørensen, D. V. Fedorov, and A. S. Jensen, *Phys. Rev. Lett.* **89**, 173002 (2002).
- [54] F. Werner and Y. Castin, *Phys. Rev. A* **74**, 053604 (2006).
- [55] S. T. Rittenhouse and C. H. Greene, *cond-mat/0702161* (2007).
- [56] Y. Castin, *C. R. Phys.* **5**, 407 (2004).
- [57] J. P. D’Incao and B. D. Esry, *Phys. Rev. Lett.* **94**, 213201 (2005).
- [58] J. E. Thomas, J. Kinast, and A. Turlapov, *Phys. Rev. Lett.* **95**, 120402 (2005).
- [59] J. von Stecher and C. H. Greene, *Phys. Rev. Lett.* **99**, 090402 (2007).
- [60] K. Singer, *Proc. R. Soc. London, Ser. A* **258**, 412 (1960).
- [61] Y. Suzuki and K. Varga, *Stochastic Variational Approach to Quantum-Mechanical Few-Body Problems* (Springer-Verlag, Berlin, 1998).
- [62] P. J. Reynolds, D. M. Ceperley, B. J. Alder, and W. A. Lester, Jr., *J. Chem. Phys.* **77**, 5593 (1982).
- [63] B. L. Hammond, W. A. Lester, Jr., and P. J. Reynolds, *Monte Carlo Methods in Ab Initio Quantum Chemistry* (World Scientific, Singapore, 1994).
- [64] G. E. Astrakharchik, J. Boronat, J. D. Casulleras, and S. Giorgini, *Phys. Rev. Lett.* **93**, 200404 (2004).
- [65] J. P. Bouchaud, A. Georges, and C. Lhuillier, *J. Phys. (Paris)* **49**, 553 (1988).
- [66] S. Y. Chang and G. F. Bertsch, *Phys. Rev. A* **76**, 021603 (R) (2007).
- [67] P. A. Whitlock, D. M. Ceperley, G. V. Chester, and M. H. Kalos, *Phys. Rev. B* **19**, 5598 (1979).
- [68] R. N. Barnett, P. J. Reynolds, and W. A. Lester, Jr., *J. Comput. Phys.* **96**, 258 (1991).
- [69] J. Casulleras and J. Boronat, *Phys. Rev. B* **52**, 3654 (1995).
- [70] S. Y. Chang and V. R. Pandharipande, *Phys. Rev. Lett.* **95**, 080402 (2005).
- [71] P. A. Skorniakov and K. A. Ter-Martirosian, *Zh. Eksp. Teor. Fiz.* **31**, 775 (1956) [*Sov. Phys. JETP* **4**, 648 (1957)].
- [72] D. S. Petrov, *Phys. Rev. A* **67**, 010703 (2003).
- [73] D. Blume and C. H. Greene, *Phys. Rev. A* **65**, 043613 (2002).
- [74] E. L. Bolda, E. Tiesinga, and P. S. Julienne, *Phys. Rev. A* **66**, 013403 (2002).
- [75] M. Brack and R. K. Bhaduri, *Semiclassical Physics* (Addison-Wesley, Reading, MA, 1997).
- [76] A. Bulgac, *Phys. Rev. A* **76**, 040502(R) (2007).
- [77] J. von Stecher and C. H. Greene, *Phys. Rev. A* **75**, 022716 (2007).
- [78] G. E. Astrakharchik, D. Blume, and S. Giorgini, unpublished; see also Sec. IXD of Ref. [11].
- [79] T. D. Son, *cond-mat/0707.1851* (2007).
- [80] M. W. Zwierlein, C. H. Schunck, A. Schirotzek, and W. Ketterle, *Nature* **442**, 54 (2006).
- [81] G. P. Partridge, W. H. Li, R. I. Kamar, Y. A. Liao, and R. G. Hulet, *Science* **311**, 503 (2006).